



A two-step method to derive combined Fourier-wavelet spectra from space-time data for studying planetary-scale waves, and its Matlab and Python software (cfw v1.0)

Yosuke Yamazaki

Leibniz Institute of Atmospheric Physics at the University of Rostock
Schlossstraße 6, 18225 Kühlungsborn

Correspondence: Y. Yamazaki (yamazaki@iap-kborn.de)

Abstract. The combined Fourier-wavelet (CFW) transform is a useful technique to characterize planetary-scale waves, such as tides and traveling planetary waves in the Earth's atmosphere. A CFW spectrum, presented in a time versus period diagram, can be used to identify wave activity that is localized in time, similar to a wavelet spectrum. A CFW spectrum can be obtained for each of eastward- and westward-propagating wave components with different zonal wavenumbers. This paper introduces an easy-to-implement method to derive CFW spectra in two steps. In the first step, the Fourier transform is performed in space (longitude), and time series of the space Fourier coefficients are derived. In the second step, the wavelet transform is performed on these time series, and wavelet coefficients are derived. It is shown that the CFW transform can be easily derived from these wavelet coefficients. The results suggest that existing Fourier and wavelet software can be utilized to derive CFW spectra. Matlab and Python scripts are created and made available at <https://igit.iap-kborn.de/yy01/cfw> that compute CFW spectra using the wavelet software provided by Torrence and Compo (1998). Some application examples are presented using longitude-time data from atmospheric and geomagnetic-field models.

1 Introduction

1.1 Background and motivation

The Earth's atmosphere can support various types of planetary-scale waves, which zonally extend around a full circle of latitude. Zonal wavenumber is defined as the number of wave cycles that fit within the latitude circle. As the wave propagates eastward or westward, an oscillation is observed at ground stations. The period of the oscillation depends on the zonal phase velocity and zonal wavenumber of the wave,

$$T = \omega^{-1} = \frac{2\pi R_E}{kC} \cos \phi, \quad (1)$$

where T (in s) is the wave period, ω (in s^{-1}) is the wave frequency, R_E (in m) is the Earth's radius, k is the zonal wavenumber, C (in m s^{-1}) is the phase speed, and ϕ (in rad) is the latitude.

Examples of planetary-scale waves in the atmosphere include atmospheric tides (Lindzen and Chapman, 1969; Forbes, 1984) and traveling planetary waves (Salby, 1984; Madden, 2007). Solar tides, with primary periods at 24 h and 12 h (called



‘diurnal’ and ‘semidiurnal’ tides, respectively), are thermally excited through periodic absorption of solar radiation mainly in the troposphere and stratosphere (Forbes, 1982a, b). Dominant modes are the westward-propagating migrating (or Sun-synchronous) diurnal tide with zonal wavenumber 1 (DW1) and migrating semidiurnal tide with zonal wavenumber 2 (SW2). Besides, non-migrating (or non-Sun-synchronous) modes are also commonly observed, such as eastward-propagating diurnal tides with zonal wavenumber 3 (DE3) and 2 (DE2) (e.g., Hagan and Forbes, 2002; Forbes et al., 2008; Oberheide et al., 2011). Tides propagate vertically upward from the source region. Their amplitude increases with height due to the reduction of atmospheric density, until dissipation eventually takes place in the mesosphere and lower thermosphere (MLT) and prevents their further growth. As a result, the wave amplitude is often largest in the MLT region.

Traveling planetary waves have a period longer than a day and shorter than several weeks. Some are interpreted as Rossby normal modes, which are predicted by classical wave theory (e.g., Longuet-Higgins, 1968; Kasahara, 1976). Rossby normal modes are solutions to Laplace’s tidal equation in an idealized atmosphere with no dissipation and mean winds, and represent free (or resonant) oscillations of the atmosphere (Forbes et al., 1995b). The oscillations that are most commonly observed in the MLT region have periods about 5–7 days (Hirota and Hirooka, 1984; Wu et al., 1994; Forbes and Zhang, 2017; Qin et al., 2021b), 9–11 days (Hirooka and Hirota, 1985; Forbes and Zhang, 2015) and 14–16 days (Forbes et al., 1995a; Day et al., 2011). They are all westward-propagating with zonal wavenumber 1, and called quasi-6-day wave (Q6DW), quasi-10-day wave (Q10DW) and quasi-16-day wave (Q16DW), respectively. Also in this category are the westward-propagating quasi-28-day wave (Q28DW) with zonal wavenumber 1 (Zhao et al., 2019), the westward-propagating quasi-4-day wave (Q4DW) with zonal wavenumber 2 (Ma et al., 2020; Yamazaki et al., 2021) and the westward-propagating quasi-7-day wave (Q7DW) with zonal wavenumber 2 (Pogoreltsev et al., 2002). The westward-propagating quasi-2-day wave (Q2DW) with zonal wavenumber 2–4 is also frequently observed in the MLT region (Wu et al., 1993; Gu et al., 2013; Moudden and Forbes, 2014; He et al., 2021), and is sometimes regarded as manifestation of mixed Rossby-gravity modes (e.g., Salby, 1981a; Salby and Callaghan, 2001). Although theoretical Rossby normal modes and mixed Rossby-gravity modes are westward-propagating, observations sometimes show eastward propagating components around the same period range (e.g., Palo et al., 2007; McDonald et al., 2011; Pancheva et al., 2018; Huang et al., 2021; Fan et al., 2022). Equatorial Kelvin waves (Matsuno, 1966; Holton and Lindzen, 1968) are equatorially-trapped eastward-propagating waves. At MLT heights, the ultra-fast Kelvin wave (UFKW) with zonal wavenumber 1 and a period of ~ 3 days is frequently detected (e.g., Lieberman and Riggin, 1997; Forbes et al., 2009; Davis et al., 2012; Gasperini et al., 2015; Yamazaki et al., 2020b).

Neither tides nor traveling planetary waves are stationary. Generally, their amplitude varies with season. Besides, tidal amplitude shows marked day-to-day variability in the MLT region (e.g., Miyoshi and Fujiwara, 2003; Pedatella et al., 2012a; Wang et al., 2021b). This can be attributed to the interaction of tidal waves with the mean flow and other waves (e.g., Chang et al., 2011; Lieberman et al., 2015; Siddiqui et al., 2022) as well as to changes in the source of tides (e.g., Miyoshi, 2006; Siddiqui et al., 2019). Enhanced tidal variability is predicted to occur in the MLT region during sudden stratospheric warming events (e.g., Fuller-Rowell et al., 2010; Pedatella et al., 2012b; Jin et al., 2012). A sudden stratospheric warming is a large-scale meteorological disturbance, which usually occurs in the winter polar stratosphere (e.g., Butler et al., 2015; Baldwin

et al., 2021). It can affect the whole atmosphere including different latitudes and height regions (e.g., Pedatella et al., 2018; Goncharenko et al., 2021).

60 Traveling planetary waves in the MLT region sometimes show a burst of wave activity that lasts for a few wave cycles. This can be attributed to changes in the zonal mean state of the atmosphere, which controls propagation conditions, atmospheric instability, and critical layers (e.g., Salby, 1981b, c; Liu et al., 2004; Yue et al., 2012; Gan et al., 2018). Large amplification of traveling planetary waves is sometimes observed following sudden stratospheric warming events (e.g., Sassi et al., 2012; Chandran et al., 2013; Gu et al., 2016; Yamazaki and Matthias, 2019; He et al., 2020; Wang et al., 2021a).

65 The MLT weather is highly variable due to the presence of various planetary-scale waves and other waves from the lower layers (e.g., Fuller-Rowell et al., 2008; Jin et al., 2011; Liu, 2014). Understanding wave activity in the MLT region is important because it has a significant impact on the region above, i.e., the ionosphere and thermosphere (IT) (e.g., Liu, 2016; Yiğit and Medvedev, 2015). The IT region is where many space infrastructures operate, and is important for the radio communication between the ground and satellites (Schunk and Sojka, 1996; Moldwin, 2022). Many studies have found wave-like signatures in the IT region that correlate with tidal and traveling planetary wave activity in the MLT region (e.g., Laštovička, 2006; 70 Immel et al., 2006; Oberheide et al., 2009; Pancheva and Mukhtarov, 2010; Gu et al., 2014; Yamazaki, 2018; Gan et al., 2020; Sobkhiz-Miandehi et al., 2022). This is the motivation behind the present study, which introduces a simple spectral analysis method to evaluate planetary-scale wave activity.

The main objective of this study is to describe an easy-to-implement method to derive ‘wavelet-like’ spectra using longitude-time data. The wavelet analysis is a multiresolution analysis technique, which is widely used in research fields including the 75 Earth science (e.g., Kumar and Foufoula-Georgiou, 1997; Torrence and Compo, 1998). A wavelet transform can be performed on time-series data to derive a ‘wavelet spectrum’, which is usually presented in a time versus period diagram. The wavelet analysis is useful for identifying wave activity that is localized in time. This feature would also be useful for studying planetary-scale waves in the MLT region, whose amplitude is variable. However, the standard wavelet technique is not directly applicable to longitude-time data, which are required for the characterization of planetary-scale waves. For spectral analysis of longitude-time data, Hayashi (1971) described a Fourier-based technique. In this study, Hayashi’s method is combined with the wavelet 80 technique so that it can detect planetary-scale wave activity that is localized in time.

1.2 Fourier-based analysis of space-time data

Hayashi (1971) proposed a Fourier-based spectral analysis method for longitude-time data, which was successfully implemented in later studies (e.g., Mechoso and Hartmann, 1982; Wheeler and Kiladis, 1999; Miyoshi and Fujiwara, 2006; Akmaev 85 et al., 2008; Sassi et al., 2016). The technique involves two steps. In the first step, the Fourier transform is performed in space (longitude), and time series of the sine and cosine Fourier coefficients are derived. In the second step, the Fourier transform is performed on these time series. Hayashi (1971) clarified how the amplitude and phase of eastward- and westward-propagating waves are related to the Fourier coefficients obtained from the second Fourier transform. What follows is a brief review of the technique of Hayashi (1971).



90 Assuming that perturbations of an atmospheric parameter W (denoted by δW) at a fixed latitude can be expressed as the sum of eastward- and westward-propagating components with various zonal wavenumbers k ($= 0, 1, 2, \dots$) and frequencies ω (>0):

$$\delta W = \sum_k \delta W_k = \sum_k (\delta W_k^+ + \delta W_k^-), \quad (2)$$

where

95
$$\delta W_k^+ = \sum_\omega R_{k,\omega}^+ \cos(\omega t - k\lambda - \varphi_{k,\omega}^+) \quad (3)$$

represents eastward-propagating components, and

$$\delta W_k^- = \sum_\omega R_{k,\omega}^- \cos(\omega t + k\lambda - \varphi_{k,\omega}^-) \quad (4)$$

is the westward-propagating counterpart. t and λ are time (in s) and longitude (in rad), respectively. R and φ are the amplitude and phase of the wave component, respectively, with the superscripts $+$ and $-$ indicating the eastward- and westward-propagating components, respectively. The above equations can be rearranged, and the component with zonal wavenumber k can be written as

100
$$\delta W_k = C_k(t) \cos kx + S_k(t) \sin kx, \quad (5)$$

with

$$C_k(t) = \sum_\omega (A_{k,\omega} \cos \omega t + B_{k,\omega} \sin \omega t) \quad (6)$$

105
$$S_k(t) = \sum_\omega (a_{k,\omega} \cos \omega t + b_{k,\omega} \sin \omega t), \quad (7)$$

where

$$A_{k,\omega} = R_{k,\omega}^+ \cos \varphi_{k,\omega}^+ + R_{k,\omega}^- \cos \varphi_{k,\omega}^- \quad (8)$$

$$B_{k,\omega} = R_{k,\omega}^+ \sin \varphi_{k,\omega}^+ + R_{k,\omega}^- \sin \varphi_{k,\omega}^- \quad (9)$$

$$a_{k,\omega} = -R_{k,\omega}^+ \sin \varphi_{k,\omega}^+ + R_{k,\omega}^- \sin \varphi_{k,\omega}^- \quad (10)$$

110
$$b_{k,\omega} = R_{k,\omega}^+ \cos \varphi_{k,\omega}^+ - R_{k,\omega}^- \cos \varphi_{k,\omega}^- \quad (11)$$

Equations (8)–(11) can be further rearranged as follows:

$$R_{k,\omega}^\pm \cos \varphi_{k,\omega}^\pm = \frac{1}{2} (A_{k,\omega} \pm b_{k,\omega}) \quad (12)$$

$$R_{k,\omega}^\pm \sin \varphi_{k,\omega}^\pm = \frac{1}{2} (B_{k,\omega} \mp a_{k,\omega}), \quad (13)$$



from which R and φ can be derived as:

$$115 \quad R_{k,\omega}^{\pm} = \frac{1}{2} \sqrt{(A_{k,\omega} \pm b_{k,\omega})^2 + (B_{k,\omega} \mp a_{k,\omega})^2} \quad (14)$$

$$\varphi_{k,\omega}^{\pm} = \arctan \frac{B_{k,\omega} \mp a_{k,\omega}}{A_{k,\omega} \pm b_{k,\omega}} \quad (15)$$

$R_{k,\omega}^{\pm}$ and $\varphi_{k,\omega}^{\pm}$ can be determined using longitude-time data sampled at a fixed latitude by, first, performing the Fourier transform in longitude to obtain time series of the sine and cosine Fourier coefficients (i.e., $S_k(t)$ and $C_k(t)$) and, then, performing the Fourier transform on $S_k(t)$ and $C_k(t)$ to obtain the sine and cosine Fourier coefficients (i.e., $B_{k,\omega}$, $b_{k,\omega}$, $A_{k,\omega}$ and $a_{k,\omega}$).

1.3 Wavelet analysis of time series

The wavelet analysis method considered here is the continuous wavelet transform described by Torrence and Compo (1998). For a given time series $x(t)$, the continuous wavelet transform X is defined as the convolution of $x(t)$ with a wavelet function Ψ :

$$125 \quad X(s, \tau) = \int_{-\infty}^{\infty} x(t) \Psi^* \left(\frac{t - \tau}{s} \right) dt, \quad (16)$$

where s is the scaling factor, representing the extent of dilation or compression of the wavelet, and τ is the translation factor, representing time shift. Ψ^* is the complex conjugate of Ψ . For the present study, the Morlet wavelet is used for Ψ . The Morlet wavelet is the product of a complex sinusoid and a Gaussian window. That is,

$$\Psi \left(\frac{t}{s} \right) = \left(\cos \frac{\omega_0 t}{s} + i \sin \frac{\omega_0 t}{s} \right) e^{-\frac{1}{2} \left(\frac{t}{s} \right)^2}. \quad (17)$$

130 ω_0 is usually set to be 6 to satisfy the admissibility condition (e.g., Farge et al., 1992).

If $x(t)$ is sampled with the sampling interval Δt ,

$$t_n = n \Delta t \quad (18)$$

$$x_n = x(n \Delta t) \quad (19)$$

$$\Psi_{n,s} = \Psi \left(\frac{n \Delta t}{s} \right) \quad (20)$$

135 where $n = \{0, 1, 2, \dots, N-1\}$, and N is the number of points in the time series. The wavelet transform (16) can be approximated as follows:

$$X_{n,s} = X(s, n \Delta t) = \sum_{n'=0}^{N-1} x_{n'} \Psi_{n'-n,s}^* \quad (21)$$

In practical application, the equation (21) is not directly used for the computation of X . Instead, the Fourier transforms of x are used in light of the convolution theorem. The convolution theorem states that the Fourier transform of a convolution



140 of two functions is the same as the product of the Fourier transforms of the two functions. The discrete Fourier transform of x is:

$$\hat{x}_m = \mathcal{F}\{x_n\} = \sum_{n=0}^{N-1} x_n e^{-i \frac{mn}{N}}, \quad (22)$$

where $m = \{0, 1, 2, \dots, N-1\}$ is the frequency index, and \mathcal{F} is the Fourier transform operator. The Fourier transform of the Morlet wavelet Ψ is:

$$145 \quad \hat{\Psi}(s\omega) = H(\omega) e^{-\frac{(s\omega - \omega_0)^2}{2}}, \quad (23)$$

where $H(\omega) = 1$ for $\omega > 0$, and $H(\omega) = 0$ for $\omega \leq 0$. The discrete Fourier transform is

$$\hat{\Psi}_m = \mathcal{F}\{\Psi_n\} = \hat{\Psi}(s\omega_m), \quad (24)$$

where

$$\omega_m = \frac{2\pi m}{N\Delta t} \quad (m \leq \frac{N}{2}) \quad (25)$$

$$150 \quad \omega_m = -\frac{2\pi m}{N\Delta t} \quad (m > \frac{N}{2}). \quad (26)$$

Based on the convolution theorem, the convolution integral of the two functions is the inverse Fourier transform of the product of the Fourier transforms of the two functions. Thus, the equation (21) can be written as:

$$X_{n,s} = \mathcal{F}^{-1}\{\hat{x}_m \hat{\Psi}_m\}, \quad (27)$$

where \mathcal{F}^{-1} is the operator for the inverse Fourier transform. Thanks to the fast Fourier transform (FFT) algorithm (e.g., Frigo
 155 and Johnson, 1998), the computation of (27) is much faster than the computation of (21).

A wavelet spectrum can be obtained by plotting the amplitude $|X_{n,s}|$ or power $|X_{n,s}|^2$ of the wavelet transform as a function of time (i.e., $n\Delta t$) and wave period (or scale s). According to Meyers et al. (1993), there is a simple relationship between the wave period T and Morlet wavelet scale s :

$$T = \frac{4\pi}{\omega_0 + \sqrt{\omega_0^2 + 2}} s. \quad (28)$$

160 Thus, $T = 1.03$ s for $\omega_0=6$.

1.4 Combined Fourier wavelet analysis

As described in 1.2, Hayashi's method involves two steps. The first step is the Fourier transform of space-time data in longitude, and the second step is the Fourier transform of the obtained Fourier coefficients in time. This paper explains how the second step (Fourier analysis in time) can be replaced by the wavelet analysis. It should be noted that the idea of using the wavelet technique
 165 in space-time analysis itself is not new. For instance, Alexander and Shepherd (2010) used the method of Hayashi (1971) to



determine the amplitude of eastward- and westward-propagating planetary-scale waves with different zonal wavenumbers, and then applied the wavelet analysis to the amplitude time series. Mukhtarov et al. (2010) performed least-squares fits of functions in the form of $R_{k,\omega} \cos(\omega t - k\lambda - \phi_{k,\omega})$ tapered by a Gaussian window. They called their technique ‘wavelet-periodogram method’. Kikuchi and Wang (2010) used a 2-dimensional (2-D) wavelet transform to analyze longitude-time data, which enables to identify wave activity that is localized not only in time but also in space. Kikuchi (2014) introduced a simpler version of the technique called ‘combined Fourier-wavelet (CFW) transform’, which involves the Fourier transform in longitude and wavelet transform in time. Kikuchi (2014) provided a Fortran software. However, since the main focus of Kikuchi (2014) was on the introduction of the CFW concept, rather than the implementation technique, the application of the CFW technique is still generally challenging for non-Fortran users.

The present study introduces an easy-to-implement method, named ‘two-step method’, for deriving CFW spectra. It allows to compute CFW spectra using existing software of Fourier and wavelet transforms, which are readily available in many data analysis software such as Matlab.

2 Methodology

In Hayashi’s method, the wave amplitude is assumed to be constant. In order to taken into account localization of wave activity, the sinusoids in (3) and (4) are replaced by Gaussian-modulated sinusoids. That is,

$$\delta W_k'^+ = \sum_{\omega} R_{k,\omega}'^+ e^{-\frac{t^2}{2}} \cos\left(\omega t - k\lambda - \varphi_{k,\omega}'^+\right) \quad (29)$$

and

$$\delta W_k'^- = \sum_{\omega} R_{k,\omega}'^- e^{-\frac{t^2}{2}} \cos\left(\omega t + k\lambda - \varphi_{k,\omega}'^-\right) \quad (30)$$

Accordingly, (6) and (7) are modified as follows:

$$C_k'(t) = \sum_{\omega} \left(A_{k,\omega}' e^{-\frac{t^2}{2}} \cos \omega t + B_{k,\omega}' e^{-\frac{t^2}{2}} \sin \omega t \right) \quad (31)$$

$$S_k'(t) = \sum_{\omega} \left(a_{k,\omega}' e^{-\frac{t^2}{2}} \cos \omega t + b_{k,\omega}' e^{-\frac{t^2}{2}} \sin \omega t \right). \quad (32)$$

In analogy to Hayashi’s formulas (8–15), the coefficients $A_{k,\omega}'$, $B_{k,\omega}'$, $a_{k,\omega}'$ and $b_{k,\omega}'$ are related to $R_{k,\omega}'^{\pm}$ and $\varphi_{k,\omega}'^{\pm}$ as follows:

$$R_{k,\omega}'^{\pm} = \frac{1}{2} \sqrt{\left(A_{k,\omega}' \pm b_{k,\omega}' \right)^2 + \left(B_{k,\omega}' \mp a_{k,\omega}' \right)^2} \quad (33)$$

$$\varphi_{k,\omega}'^{\pm} = \arctan \frac{B_{k,\omega}' \mp a_{k,\omega}'}{A_{k,\omega}' \pm b_{k,\omega}'}. \quad (34)$$

Using (17), equations (31) and (32) can be expressed as:

$$C_k'(t) = \sum_{\omega} \left(A_{k,\omega}' \Re(\Psi^*) - B_{k,\omega}' \Im(\Psi^*) \right) \quad (35)$$

$$S_k'(t) = \sum_{\omega} \left(a_{k,\omega}' \Re(\Psi^*) - b_{k,\omega}' \Im(\Psi^*) \right), \quad (36)$$



where $\Re(\Psi^*)$ and $\Im(\Psi^*)$ represent the real and imaginary parts of Ψ^* , respectively. Just like $A_{k,\omega}$ and $B_{k,\omega}$ which can be obtained as the cosine and sine coefficients of the Fourier transform of C_k (see (6)), $A'_{k,\omega}$ and $B'_{k,\omega}$ can be obtained as the real and negative imaginary coefficients of the wavelet transform of C'_k . Similarly, $a'_{k,\omega}$ and $b'_{k,\omega}$ can be obtained as the real and negative imaginary coefficients of the wavelet transform of S'_k .

In summary, the amplitude R' and phase φ' of eastward (+) and westward (−) propagating wave components with zonal wavenumber k and frequency ω can be determined in the following two steps. The first step is the Fourier transform of longitude-time data in longitude, which gives the time series of the cosine and sine Fourier coefficients (i.e., $C'_k(t)$ and $S'_k(t)$). The second step is the wavelet transform of $C'_k(t)$ and $S'_k(t)$ in time. The real part of the wavelet coefficients of $C'_k(t)$ and $S'_k(t)$ gives $A'_{k,\omega}$ and $a'_{k,\omega}$, respectively; and the negative imaginary part of the wavelet coefficients of $C'_k(t)$ and $S'_k(t)$ gives $B'_{k,\omega}$ and $b'_{k,\omega}$, respectively. Once $A'_{k,\omega}$, $B'_{k,\omega}$, $a'_{k,\omega}$ and $b'_{k,\omega}$ are determined, $R'_{k,\omega}^{\pm}$ and $\varphi'_{k,\omega}^{\pm}$ can be derived using (33) and (34).

The implementation of the technique is easy, as it requires only standard Fourier and wavelet tools. Matlab and Python software are created and made available at <https://igit.iap-kborn.de/yy01/cfw> that compute $R'_{k,\omega}^{\pm}$ and $\varphi'_{k,\omega}^{\pm}$ for input data evenly gridded in time and longitude. For the Fourier analysis, the FFT algorithm is used when there are no missing values in the input data; otherwise, the least-squares method (e.g., Wells et al., 1985) is used, which allow gaps in the input data. The wavelet analysis is based on the software provided by Torrence and Compo (1998), which outputs not only the wavelet transform but also other useful parameters such as the ‘cone of influence’ and the threshold for the 95% confidence level.

3 Application examples

In this section, five examples are presented for the application of the two-step method of the CFW analysis to space-time data. The first example uses synthetic data, for which the exact wave composition is known. In the second, third and fourth examples, longitude-time data from atmospheric models are analyzed to demonstrate that the technique can be used to identify planetary-scale waves in the MLT region. In the last example, longitude-time data from a model of the Earth’s magnetic field are analyzed. This is to demonstrate that the technique can be used outside the field of atmospheric science.

For the analysis of atmospheric waves, special attention is paid to sudden stratospheric warming events, where tides and traveling planetary waves in the MLT region often show a large response. The events that are well documented in the literature are selected. In earlier studies, a Fourier-based method is most commonly used for examining planetary-scale wave activity during sudden stratospheric warmings. It is possible to evaluate time variations of tides and traveling planetary waves by applying a 2-D Fourier transform to a short-time segment of data and moving the analysis window in time (e.g., Jin et al., 2012). The advantage of the CFW transform is that the computation of spectra is much faster, because it reduces iterative calculations by the use of the convolution theorem and FFT algorithm (see Section 1.3).

3.1 Analysis of synthetic data

A 2-D data matrix is created that mimics longitude-time data containing planetary-scale waves. The data, presented in Figure 1a, consist of two wave components, namely ‘wave_A’ and ‘wave_B’, along with noise. The wave_A is westward-propagating



225 with zonal wavenumber $k=2$ (W2) and the wave_B is eastward-propagating with zonal wavenumber $k=3$ (E3). Notations such as W2 and E3 are used in the remainder of this paper, where ‘W’ and ‘E’ denote westward- and eastward-propagating components, respectively, and the number that follows W or E represents the zonal wavenumber k .

The amplitude of wave_A is depicted in the upper panel of Figure 1b. It changes between 0 and 1 over time in an arbitrary manner. The period of wave_A also changes over time, as shown in the lower panel of Figure 1b. Also presented in the
230 lower panel of Figure 1b is the CFW amplitude spectrum for the W2 component, as derived using the two-step method. The white curves indicate the 95% significance level estimated using the method described by Torrence and Compo (1998). The white dashed lines show the cone of influence, outside of which the edge effect may not be negligible. The CFW spectrum successfully identifies spectral peaks at the period of wave_A. The spectral amplitude tends to exceed the significance threshold when the amplitude of wave_A is above 0. Figure 1c is similar to Figure 1b except for wave_B. Again, the CFW spectrum
235 succeeds to identify the amplitude and period of wave_B.

3.2 GAIA simulation: Tides and traveling planetary waves during August–October 2019

There was an Antarctic sudden stratospheric warming in September 2019 (Lim et al., 2020; Rao et al., 2020; Yamazaki et al., 2020a). Although this event is categorized as a ‘minor’ warming (i.e., no reversal of the zonal mean flow at 10 hPa), it was unusually strong for a Southern-Hemisphere event in various measures (Lim et al., 2021), and its effects were observed at
240 different layers of the atmosphere (e.g., Goncharenko et al., 2020; Noguchi et al., 2020; Safieddine et al., 2020; Wargan et al., 2020; Yamazaki et al., 2020a). A global simulation of the September 2019 sudden stratospheric warming event was presented by Miyoshi and Yamazaki (2020) based on the whole atmosphere model GAIA. GAIA stands for the Ground-to-Topside Model of Atmosphere and Ionosphere for Aeronomy, and detailed model descriptions can be found in Jin et al. (2011) and Miyoshi et al. (2017). Figure 2a shows the polar stratospheric temperature and zonal mean zonal wind velocity at 60°N at
245 10 hPa during August–October, as derived from the GAIA model. A rapid increase of the polar temperature in September and concurrent reduction of the zonal mean zonal wind velocity are evident, which indicates the occurrence of the sudden stratospheric warming. Since the model is constrained by the JRA55 reanalysis (Kobayashi et al., 2015) below a height of 40 km, these results strongly reflect the JRA55 predictions.

Figure 2b depicts hourly values of the zonal wind velocity over the equator at an altitude of 100 km as a function of time
250 and longitude. The zonal wind velocity shows considerable variability within the range of ± 200 m/s, which is mostly due to waves generated in the region below 40 km. Figures 2c–2h show CFW spectra of the equatorial zonal wind velocity at 100 km for different wave components.

In Figure 2c, the amplitude of the W1 component at a period T of ~ 6 days is enhanced around Days 40–70. Earlier studies found that the amplitude of the Q6DW (W1, $T \sim 6$ days) during the September 2019 sudden stratospheric warming was un-
255 usually large compared to its seasonal climatology and had a significant impact on the ionosphere (Lin et al., 2020; Gu et al., 2021; Lee et al., 2021; Ma et al., 2022b; Qin et al., 2021a; Yamazaki et al., 2020a; Miyoshi and Yamazaki, 2020; Mitra et al., 2022). In Figure 2e, there is also a hint of the enhanced Q4DW (W2, $T \sim 4$ days) and Q7DW (W2, $T \sim 7$ days) around the same time.



In Figure 2d, the UFKW (E1, $T \sim 3.5$ days) is seen throughout the period. In Figure 2g, the Q2DW (W3, $T \sim 2$ days) is seen
260 at the beginning of August 2019, but its amplitude is below the significance threshold. Their wave activity seems unrelated to
the occurrence of the sudden stratospheric warming. Also, there is no apparent correlation between the sudden stratospheric
warming and tidal activity. The most prominent tidal mode in these figures is DE3 (Figure 2h). The amplitude of DE3 is known
to be largest during August–October (e.g., Akmaev et al., 2008; Zhang et al., 2006).

3.3 SD/WACCM-X simulation: Tidal variability during January–February 2009

265 A ‘major’ Arctic sudden stratospheric warming occurred in January 2009 (Manney et al., 2009; Harada et al., 2010). Whole
atmosphere simulations of this event were presented by several authors (e.g., Fuller-Rowell et al., 2011; Jin et al., 2012; Sassi
et al., 2013; Pedatella et al., 2014; Siddiqui et al., 2021). Siddiqui et al. (2021) used the Whole Atmosphere Community Climate
Model with thermosphere and ionosphere extension (WACCM-X) (Liu et al., 2018) with specified dynamics (SD), in which
the region below 50 km is constrained by the Modern Era Retrospective Analysis for Research and Applications Version 2
270 (MERRA-2) (Gelaro et al., 2017). The polar temperature and zonal mean zonal wind velocity at 60°N at 10 hPa derived from
this SD/WACCM-X simulation are plotted in Figure 3a for the period of January–February 2009. The reversal of the zonal
mean flow is seen on Day 23, confirming that this event is a major warming.

Observational studies have found large semidiurnal variations in the ionosphere during the January 2009 sudden stratospheric
warming (Goncharenko et al., 2010a, b; Fejer et al., 2010; Yue et al., 2010). Numerical studies clarified that the semidiurnal
275 ionospheric variations are due to the enhancement of semidiurnal tides that are generated in the lower atmosphere and propagate
into the ionosphere (Jin et al., 2012; Wang et al., 2014; Pedatella et al., 2014). Figure 3b shows the W2 component of the CFW
spectrum for the zonal wind velocity at 50°N and 110 km. An enhancement of SW2 (W2, $T=12$ h) is clearly visible following
the reversal of the zonal mean flow. By performing the CFW analysis at different latitudes, it is possible to visualize the global
structure of SW2 (Figure 3c). It can be seen from Figure 3c that the amplitude of SW2 increased and decreased in the Northern
280 and Southern Hemispheres, respectively, during the sudden stratospheric warming. A similar plot is shown in Figure 3d but
for DW1 (W1, $T=24$ h) and at 95 km, where the amplitude of DW1 is largest. The relationship between sudden stratospheric
warmings and DW1 tidal variability was discussed in Siddiqui et al. (2022).

3.4 SD/WACCM-X simulation: Traveling planetary waves during January–May 2016

A sudden stratospheric warming that coincides with the spring transition is called a ‘final’ warming (e.g. Black and McDaniel,
285 2007; Matthias et al., 2021). Studies have noted that a final warming event is often accompanied by a strong Q10DW (W1,
 $T \sim 10$ days) in the MLT region (Yamazaki and Matthias, 2019; Yu et al., 2019; Yin et al., 2022; Qin et al., 2022). Examples
include the final warming event in March 2016. Figure 4a shows the polar temperature and zonal mean zonal wind velocity at
10 hPa as obtained from the SD/WACCM-X simulation presented by Gasperini et al. (2020). The direction of the zonal mean
flow reversed from eastward to westward on Day 65, and did not turn back eastward until the next winter.

290 Figure 4b displays daily values of the geopotential height at 0.01 hPa (~ 77 km) as a function of time and longitude, where
a westward-propagating wave-like perturbation is visible during the final warming. The W1 and E1 components of the CFW



spectrum obtained from these data are presented in Figures 4c and 4d, respectively. A burst of the Q10DW (W1, $T \sim 10$ days) during the final warming can be easily identified in the W1 spectrum (Figure 4c). The height profiles of the amplitude and phase of the Q10DW are depicted in Figures 4e and 4f, respectively, for Day 72. The peak of the amplitude is seen at ~ 70 km. The downward phase propagation (Figure 4f) is consistent with the upward energy propagation of the Q10DW. The characteristics of the Q10DW during the March 2016 final warming derived with the CFW method are in good agreement with the observations presented by Yamazaki and Matthias (2019) based on a least-squares Fourier technique.

As a brief summary, the results presented in Sections 3.2–3.4 demonstrate that CFW spectra derived using the two-step method described in Section 2 are useful for identifying various types of tides and traveling planetary waves in the MLT region and their temporal variability. The structures of the planetary-scale waves can be determined by performing the CFW analysis at different latitudes and heights.

3.5 CHAOS-7 geomagnetic field model: Secular acceleration during 1997–2022

The Earth's magnetic field consists of contributions from various sources (e.g., Olsen and Stolle, 2012). The main contribution comes from the 'core field' (>95% of the total field), which is caused by electric currents flowing in the Earth's core. Other contributions include the 'crustal field' due to magnetized rocks in the solid Earth (e.g., Maus et al., 2006; Thébault et al., 2016) and the 'magnetospheric field' resulting from large-scale magnetospheric currents (e.g., Lühr et al., 2017). CHAOS-7 is a data-driven model of the geomagnetic field based on magnetic field measurements on the ground and at satellites (Finlay et al., 2020). The radial component of the core field B_r at the core-mantle boundary is evaluated using CHAOS-7. The second-order time derivative of B_r is called 'secular acceleration' (SA) and is often used in the investigation of short-term variations in the core field (e.g., Bloxham et al., 2002; Chulliat and Maus, 2014; Chulliat et al., 2015; Aubert and Finlay, 2019). Chulliat et al. (2015) analyzed SA data obtained from an earlier version of the CHAOS model, and examined spatio-temporal characteristics of SA at low latitudes during 2000–2015 using a 2-D Fourier transform method. Their analysis is repeated here but for the extended period 1997–2022 using the CFW technique.

Figure 5a displays monthly values of the SA over the equator as a function of time and longitude. Variations on time scales of several years are visible. Following Chulliat et al. (2015), SA data within $\pm 15^\circ$ latitudes are separated into the components that are symmetric and antisymmetric about the equator. The CFW analysis is performed on both the symmetric and antisymmetric components. Figures 5b and 5c present the global CFW spectra (i.e., the average of CFW spectra over the entire data period) for the symmetric and antisymmetric components, respectively. Oscillations with periods of 5–9 years are apparent in the symmetric component (Figures 5b). The antisymmetric component (Figure 5c) is much smaller than the symmetric component. These results are in agreement with those presented by Chulliat et al. (2015). The cause of these oscillations in SA is still under debate. Gillet et al. (2022) pointed out that the oscillations of the core field around periods of 7 years are consistent with Magneto-Coriolis eigenmodes.

In Figure 5b, the dominant modes are those with zonal wavenumbers $k=3$ and $k=5$. Interestingly, the global CFW spectrum tends to be symmetric about $k=0$. In other words, the data contain approximately the same amount of eastward- and westward-propagating waves for a given k . Implication is that the observed 5–9-year oscillation of SA is associated with standing waves



(rather than traveling waves). The possible contribution from standing waves is also addressed by Chulliat et al. (2015). A standing wave is equivalent to the superposition of eastward- and westward-propagating waves with the same amplitude. Figure 5d shows that the time evolutions of the eastward- and westward-propagating components are similar for both $k=3$ and $k=5$, further supporting that the oscillations are mainly due to standing waves. Some earlier studies discussed possible ways to separate standing waves and traveling waves in the analysis of longitude-time data (e.g., Hayashi, 1977, 1979; Pogoreltsev et al., 2002; Ma et al., 2022a). The implementation of such a technique for the CFW analysis would be a topic for a separate study.

4 Summary and Conclusions

This study describes a simple method for deriving combined Fourier-wavelet (CFW) spectra (Kikuchi, 2014) from 2-D longitude-time data. The method is conceptually similar to that of Hayashi (1971), which first performs the Fourier analysis in longitude, then performs the Fourier analysis in time. In the proposed technique, the Fourier analysis in time is replaced by the wavelet analysis (Torrence and Compo, 1998), which can resolve wave activity localized in time. Briefly, the implementation of the technique involves two steps. In the first step, the Fourier transform is performed in longitude, and time series of the sine and cosine Fourier coefficients are derived. In the second step, the wavelet transform is performed on these time series, and real and imaginary wavelet coefficients are derived. Using these wavelet coefficients, CFW spectra can be obtained separately for eastward- and westward-propagating wave components with different zonal wavenumbers (see Section 2 for details).

Matlab and Python software for computing CFW spectra using the two-step method are created and made available at <https://igit.iap-kborn.de/yy01/cfw>. Application examples, based on these CFW software, are presented in Section 3. The results suggest that the technique can successfully identify tides and traveling planetary waves in the mesosphere and lower thermosphere (MLT) region and their transient response to sudden stratospheric warming events (Sections 3.2–3.4), which in previous studies, were most commonly examined based on a short-time 2-D Fourier method using a moving window. The CFW method has an advantage in that the computation is much faster because it avoids iterative calculations that are necessary for the short-term Fourier method. An application example is also presented for a model of the Earth's magnetic field (Sections 3.5), demonstrating that the proposed CFW technique can also be useful in research areas outside atmospheric science.

Code and data availability. Matlab and Python software (cfw v1.0) for computing CFW spectra with the two-step method are available at URL: <https://igit.iap-kborn.de/yy01/cfw> under the GNU General Public License. They can also be downloaded from the Zenodo website at <https://doi.org/10.5281/zenodo.7458051>. Matlab wavelet software was provided by C. Torrence and G. Compo under the MIT license, and is available at URL: <http://atoc.colorado.edu/research/wavelets/>. Python wavelet software was created by Evgeniya Predybaylo and Michael von Papen based on Torrence and Compo (1998), and is also available at the same URL. The GAIA simulation data used in Section 3.2 are available from GFZ Data Services (<https://doi.org/10.5880/GFZ.2.3.2020.004>). The SD/WACCM-X simulation data used in Section 3.3 are available from <https://data.mendeley.com/datasets/47pnw8pgmk/1>. The SD/WACCM-X simulation data used in Section 3.4 are available



from <https://doi.org/10.26024/5b58-nc53>. The geomagnetic field model CHAOS-7 used in Section 3.5 is available from the DTU Space website (<http://www.spacecenter.dk/files/magnetic-models/CHAOS-7/>).

360 *Author contributions.* YY was in charge of conceptualizing the study, data analysis, visualization of the results, writing the manuscript, and creating the Matlab and Python scripts.

Competing interests. The author declares that he has no conflict of interest.

Acknowledgements. The author was supported by the Deutsche Forschungsgemeinschaft (DFG) grant YA-574-3-1.



References

- 365 Akmaev, R., Fuller-Rowell, T., Wu, F., Forbes, J., Zhang, X., Anghel, A., Iredell, M., Moorthi, S., and Juang, H.-M.: Tidal variability in the lower thermosphere: Comparison of Whole Atmosphere Model (WAM) simulations with observations from TIMED, *Geophys. Res. Lett.*, 35, <https://doi.org/doi:10.1029/2007GL032584>, 2008.
- Alexander, S. and Shepherd, M.: Planetary wave activity in the polar lower stratosphere, *Atmos. Chem. Phys.*, 10, 707–718, <https://doi.org/10.5194/acp-10-707-2010>, 2010.
- 370 Aubert, J. and Finlay, C. C.: Geomagnetic jerks and rapid hydromagnetic waves focusing at Earth’s core surface, *Nature Geoscience*, 12, 393–398, <https://doi.org/10.1038/s41561-019-0355-1>, 2019.
- Baldwin, M. P., Ayarzagüena, B., Birner, T., Butchart, N., Butler, A. H., Charlton-Perez, A. J., Domeisen, D. I., Garfinkel, C. I., Garny, H., Gerber, E. P., et al.: Sudden stratospheric warmings, *Rev. Geophys.*, 59, e2020RG000708, <https://doi.org/10.1029/2020RG000708>, 2021.
- Bloxham, J., Zatman, S., and Dumberry, M.: The origin of geomagnetic jerks, *Nature*, 420, 65–68, <https://doi.org/10.1038/nature01134>, 375 2002.
- Butler, A. H., Seidel, D. J., Hardiman, S. C., Butchart, N., Birner, T., and Match, A.: Defining sudden stratospheric warmings, *Bull. Am. Meteorol.*, 96, 1913–1928, <https://doi.org/10.1175/BAMS-D-13-00173.1>, 2015.
- Chandran, A., Garcia, R., Collins, R., and Chang, L.: Secondary planetary waves in the middle and upper atmosphere following the stratospheric sudden warming event of January 2012, *Geophys. Res. Lett.*, 40, 1861–1867, <https://doi.org/10.1002/grl.50373>, 2013.
- 380 Chang, L. C., Palo, S. E., and Liu, H.-L.: Short-term variability in the migrating diurnal tide caused by interactions with the quasi 2 day wave, *J. Geophys. Res.: Atmospheres*, 116, <https://doi.org/10.1029/2010JD014996>, 2011.
- Chulliat, A. and Maus, S.: Geomagnetic secular acceleration, jerks, and a localized standing wave at the core surface from 2000 to 2010, *J. Geophys. Res.: Solid Earth*, 119, 1531–1543, <https://doi.org/10.1002/2013JB010604>, 2014.
- Chulliat, A., Alken, P., and Maus, S.: Fast equatorial waves propagating at the top of the Earth’s core, *Geophys. Res. Lett.*, 42, 3321–3329, 385 <https://doi.org/10.1002/2015GL064067>, 2015.
- Davis, R. N., Chen, Y.-W., Miyahara, S., and Mitchell, N. J.: The climatology, propagation and excitation of ultra-fast Kelvin waves as observed by meteor radar, Aura MLS, TRMM and in the Kyushu-GCM, *Atmos. Chem. Phys.*, 12, 1865–1879, <https://doi.org/10.5194/acp-12-1865-2012>, 2012.
- Day, K. A., Hibbins, R. E., and Mitchell, N. J.: Aura MLS observations of the westward-propagating $s = 1$, 16-day planetary wave in the 390 stratosphere, mesosphere and lower thermosphere, *Atmos. Chem. Phys.*, 11, 4149–4161, <https://doi.org/10.5194/acp-11-4149-2011>, 2011.
- Fan, Y., Huang, C. M., Zhang, S. D., Huang, K. M., and Gong, Y.: Long-Term Study of Quasi-16-day Waves Based on ERA5 Reanalysis Data and EOS MLS Observations From 2005 to 2020, *J. Geophys. Res.: Space Physics*, 127, e2021JA030030, <https://doi.org/10.1029/2021JA030030>, 2022.
- Farge, M. et al.: Wavelet transforms and their applications to turbulence, *Annu. Rev. Fluid Mech.*, 24, 395–458, 395 <https://doi.org/10.1146/annurev.fl.24.010192.002143>, 1992.
- Fejer, B., Olson, M., Chau, J., Stolle, C., Lühr, H., Goncharenko, L., Yumoto, K., and Nagatsuma, T.: Lunar-dependent equatorial ionospheric electrodynamic effects during sudden stratospheric warmings, *J. Geophys. Res.: Space Physics*, 115, <https://doi.org/10.1029/2010JA015273>, 2010.



- 400 Finlay, C. C., Kloss, C., Olsen, N., Hammer, M. D., Tøffner-Clausen, L., Grayver, A., and Kuvshinov, A.: The CHAOS-7 geomagnetic field model and observed changes in the South Atlantic Anomaly, *Earth, Planets and Space*, 72, 1–31, <https://doi.org/10.1186/s40623-020-01252-9>, 2020.
- Forbes, J., Hagan, M., Miyahara, S., Vial, F., Manson, A., Meek, C., and Portnyagin, Y. I.: Quasi 16-day oscillation in the mesosphere and lower thermosphere, *J. Geophys. Res.: Atmospheres*, 100, 9149–9163, <https://doi.org/10.1029/94JD02157>, 1995a.
- 405 Forbes, J., Zhang, X., Palo, S., Russell, J., Mertens, C., and Mlynczak, M.: Tidal variability in the ionospheric dynamo region, *J. Geophys. Res.: Space Physics*, 113, <https://doi.org/10.1029/2007JA012737>, 2008.
- Forbes, J. M.: Atmospheric tides: 1. Model description and results for the solar diurnal component, *J. Geophys. Res.: Space Physics*, 87, 5222–5240, <https://doi.org/10.1029/JA087iA07p05222>, 1982a.
- Forbes, J. M.: Atmospheric tide: 2. The solar and lunar semidiurnal components, *J. Geophys. Res.: Space Physics*, 87, 5241–5252, <https://doi.org/10.1029/JA087iA07p05241>, 1982b.
- 410 Forbes, J. M.: Middle atmosphere tides, *J. Atmos. Terr. Phys.*, 46, 1049–1067, [https://doi.org/10.1016/0021-9169\(84\)90008-4](https://doi.org/10.1016/0021-9169(84)90008-4), 1984.
- Forbes, J. M. and Zhang, X.: Quasi-10-day wave in the atmosphere, *J. Geophys. Res.: Atmospheres*, 120, 11–079, <https://doi.org/10.1002/2015JD023327>, 2015.
- Forbes, J. M. and Zhang, X.: The quasi-6 day wave and its interactions with solar tides, *J. Geophys. Res.: Space Physics*, 122, 4764–4776, <https://doi.org/10.1002/2017JA023954>, 2017.
- 415 Forbes, J. M., Zhang, X., Palo, S. E., Russell, J., Mertens, C. J., and Mlynczak, M.: Kelvin waves in stratosphere, mesosphere and lower thermosphere temperatures as observed by TIMED/SABER during 2002–2006, *Earth, Planets and Space*, 61, 447–453, <https://doi.org/10.1186/BF03353161>, 2009.
- Forbes, J. M. et al.: Tidal and planetary waves, *The Upper Mesosphere and Lower Thermosphere: A Review of Experiment and Theory*, *Geophys. Monogr. Ser.*, 87, 67–87, <https://doi.org/10.1029/GM087p0067>, 1995b.
- 420 Frigo, M. and Johnson, S. G.: FFTW: An adaptive software architecture for the FFT, in: *Proceedings of the 1998 IEEE International Conference on Acoustics, Speech and Signal Processing, ICASSP'98 (Cat. No. 98CH36181)*, vol. 3, pp. 1381–1384, IEEE, <https://doi.org/10.1109/ICASSP.1998.681704>, 1998.
- Fuller-Rowell, T., Akmaev, R., Wu, F., Anghel, A., Maruyama, N., Anderson, D., Codrescu, M., Iredell, M., Moorthi, S., Juang, H.-M., et al.: Impact of terrestrial weather on the upper atmosphere, *Geophys. Res. Lett.*, 35, <https://doi.org/10.1029/2007GL032911>, 2008.
- 425 Fuller-Rowell, T., Wu, F., Akmaev, R., Fang, T.-W., and Araujo-Pradere, E.: A whole atmosphere model simulation of the impact of a sudden stratospheric warming on thermosphere dynamics and electrodynamics, *J. Geophys. Res.: Space Physics*, 115, <https://doi.org/10.1029/2010JA015524>, 2010.
- Fuller-Rowell, T., Wang, H., Akmaev, R., Wu, F., Fang, T.-W., Iredell, M., and Richmond, A.: Forecasting the dynamic and electrodynamic response to the January 2009 sudden stratospheric warming, *Geophys. Res. Lett.*, 38, <https://doi.org/10.1029/2011GL047732>, 2011.
- 430 Gan, Q., Oberheide, J., and Pedatella, N. M.: Sources, sinks, and propagation characteristics of the quasi 6-day wave and its impact on the residual mean circulation, *J. Geophys. Res.: Atmospheres*, 123, 9152–9170, <https://doi.org/10.1029/2018JD028553>, 2018.
- Gan, Q., Eastes, R. W., Burns, A. G., Wang, W., Qian, L., Solomon, S. C., Codrescu, M. V., and McClintock, W. E.: New observations of large-scale waves coupling with the ionosphere made by the GOLD Mission: Quasi-16-day wave signatures in the F-region OI 135.6-nm nightglow during sudden stratospheric warmings, *J. Geophys. Res.: Space Physics*, 125, e2020JA027880, <https://doi.org/10.1029/2020JA027880>, 2020.
- 435



- Gasparini, F., Forbes, J., Doornbos, E., and Bruinsma, S.: Wave coupling between the lower and middle thermosphere as viewed from TIMED and GOCE, *J. Geophys. Res.: Space Physics*, 120, 5788–5804, <https://doi.org/doi.org/10.1002/2015JA021300>, 2015.
- Gasparini, F., Liu, H., and McInerney, J.: Preliminary evidence of Madden-Julian Oscillation effects on ultrafast tropical waves in the thermosphere, *J. Geophys. Res.: Space Physics*, 125, e2019JA027 649, <https://doi.org/10.1029/2019JA027649>, 2020.
- 440 Gelaro, R., McCarty, W., Suárez, M. J., Todling, R., Molod, A., Takacs, L., Randles, C. A., Darmenov, A., Bosilovich, M. G., Reichle, R., et al.: The modern-era retrospective analysis for research and applications, version 2 (MERRA-2), *J. Clim.*, 30, 5419–5454, <https://doi.org/10.1175/JCLI-D-16-0758.1>, 2017.
- Gillet, N., Gerick, F., Jault, D., Schwaiger, T., Aubert, J., and Istas, M.: Satellite magnetic data reveal interannual waves in Earth’s core, *Proc. Natl. Acad. Sci.*, 119, e2115258 119, <https://doi.org/10.1073/pnas.2115258119>, 2022.
- 445 Goncharenko, L., Chau, J., Liu, H.-L., and Coster, A.: Unexpected connections between the stratosphere and ionosphere, *Geophys. Res. Lett.*, 37, <https://doi.org/10.1029/2010GL043125>, 2010a.
- Goncharenko, L., Coster, A., Chau, J., and Valladares, C.: Impact of sudden stratospheric warmings on equatorial ionization anomaly, *J. Geophys. Res.: Space Physics*, 115, <https://doi.org/10.1029/2010JA015400>, 2010b.
- Goncharenko, L. P., Harvey, V. L., Greer, K. R., Zhang, S.-R., and Coster, A. J.: Longitudinally dependent low-latitude ionospheric distur-
- 450 bances linked to the Antarctic sudden stratospheric warming of September 2019, *J. Geophys. Res.: Space Physics*, 125, e2020JA028 199, <https://doi.org/10.1029/2020JA028199>, 2020.
- Goncharenko, L. P., Harvey, V. L., Liu, H., and Pedatella, N. M.: Sudden Stratospheric Warming Impacts on the Ionosphere–Thermosphere System: A Review of Recent Progress, *Ionosphere Dynamics and Applications*, pp. 369–400, <https://doi.org/10.1002/9781119815617.ch16>, 2021.
- 455 Gu, S.-Y., Li, T., Dou, X., Wu, Q., Mlynczak, M., and Russell Iii, J.: Observations of quasi-two-day wave by TIMED/SABER and TIMED/TIDI, *J. Geophys. Res.: Atmospheres*, 118, 1624–1639, <https://doi.org/10.1002/jgrd.50191>, 2013.
- Gu, S.-Y., Dou, X., Lei, J., Li, T., Luan, X., Wan, W., and Russell III, J.: Ionospheric response to the ultrafast Kelvin wave in the MLT region, *J. Geophys. Res.: Space Physics*, 119, 1369–1380, <https://doi.org/10.1002/2013JA019086>, 2014.
- Gu, S.-Y., Liu, H.-L., Dou, X., and Li, T.: Influence of the sudden stratospheric warming on quasi-2-day waves, *Atmos. Chem. Phys.*, 16, 4885–4896, <https://doi.org/10.5194/acp-16-4885-2016>, 2016.
- 460 Gu, S.-Y., Teng, C.-K.-M., Li, N., Jia, M., Li, G., Xie, H., Ding, Z., and Dou, X.: Multivariate analysis on the ionospheric responses to planetary waves during the 2019 Antarctic SSW event, *J. Geophys. Res.: Space Physics*, 126, e2020JA028 588, <https://doi.org/10.1029/2020JA028588>, 2021.
- Hagan, M. and Forbes, J.: Migrating and nonmigrating diurnal tides in the middle and upper atmosphere excited by tropospheric latent heat
- 465 release, *J. Geophys. Res.: Atmospheres*, 107, ACL–6, <https://doi.org/10.1029/2001JD001236>, 2002.
- Harada, Y., Goto, A., Hasegawa, H., Fujikawa, N., Naoe, H., and Hirooka, T.: A major stratospheric sudden warming event in January 2009, *J. Atmos. Sci.*, 67, 2052–2069, <https://doi.org/10.1175/2009JAS3320.1>, 2010.
- Hayashi, Y.: A generalized method of resolving disturbances into progressive and retrogressive waves by space Fourier and time cross-spectral analyses, *J. Meteorol. Soc. Japan. Ser. II*, 49, 125–128, https://doi.org/10.2151/jmsj1965.49.2_125, 1971.
- 470 Hayashi, Y.: On the coherence between progressive and retrogressive waves and a partition of space-time power spectra into standing and traveling parts, *J. Appl. Meteorol. Climatol.*, 16, 368–373, [https://doi.org/10.1175/1520-0450\(1977\)016<0368:OTCBPA>2.0.CO;2](https://doi.org/10.1175/1520-0450(1977)016<0368:OTCBPA>2.0.CO;2), 1977.
- Hayashi, Y.: A generalized method of resolving transient disturbances into standing and traveling waves by space-time spectral analysis, *J. Atmos. Sci.*, 36, 1017–1029, [https://doi.org/10.1175/1520-0469\(1979\)036<1017:AGMORT>2.0.CO;2](https://doi.org/10.1175/1520-0469(1979)036<1017:AGMORT>2.0.CO;2), 1979.



- He, M., Yamazaki, Y., Hoffmann, P., Hall, C. M., Tsutsumi, M., Li, G., and Chau, J. L.: Zonal Wave Number Diagnosis
475 of Rossby Wave-Like Oscillations Using Paired Ground-Based Radars, *J. Geophys. Res.: Atmospheres*, 125, e2019JD031599,
<https://doi.org/10.1029/2019JD031599>, 2020.
- He, M., Chau, J. L., Forbes, J. M., Zhang, X., Englert, C. R., Harding, B. J., Immel, T. J., Lima, L. M., Bhaskar Rao, S. V., Ratnam, M. V.,
et al.: Quasi-2-day wave in low-latitude atmospheric winds as viewed from the ground and space during January–March, 2020, *Geophys.*
Res. Lett., 48, e2021GL093466, <https://doi.org/10.1029/2021GL093466>, 2021.
- 480 Hirooka, T. and Hirota, I.: Normal mode Rossby waves observed in the upper stratosphere. Part II: Second antisym-
metric and symmetric modes of zonal wavenumbers 1 and 2, *J. Atmos. Sci.*, 42, 536–548, [https://doi.org/10.1175/1520-0469\(1985\)042<0536:NMRWOI>2.0.CO;2](https://doi.org/10.1175/1520-0469(1985)042<0536:NMRWOI>2.0.CO;2), 1985.
- Hirota, I. and Hirooka, T.: Normal mode Rossby waves observed in the upper stratosphere. Part I: First symmetric modes of zonal wavenum-
bers 1 and 2, *J. Atmos. Sci.*, 41, 1253–1267, [https://doi.org/10.1175/1520-0469\(1984\)041<1253:NMRWOI>2.0.CO;2](https://doi.org/10.1175/1520-0469(1984)041<1253:NMRWOI>2.0.CO;2), 1984.
- 485 Holton, J. R. and Lindzen, R. S.: A note on “Kelvin” waves in the atmosphere, *Mon. Weather Rev.*, 96, 385–386, [https://doi.org/10.1175/1520-0493\(1968\)096<0385:ANOKWI>2.0.CO;2](https://doi.org/10.1175/1520-0493(1968)096<0385:ANOKWI>2.0.CO;2), 1968.
- Huang, C., Li, W., Zhang, S., Chen, G., Huang, K., and Gong, Y.: Investigation of dominant traveling 10-day wave components using
long-term MERRA-2 database, *Earth, Planets and Space*, 73, 1–12, <https://doi.org/10.1186/s40623-021-01410-7>, 2021.
- Immel, T., Sagawa, E., England, S., Henderson, S., Hagan, M., Mende, S., Frey, H., Swenson, C., and Paxton, L.: Control of equatorial
490 ionospheric morphology by atmospheric tides, *Geophys. Res. Lett.*, 33, <https://doi.org/10.1029/2006GL026161>, 2006.
- Jin, H., Miyoshi, Y., Fujiwara, H., Shinagawa, H., Terada, K., Terada, N., Ishii, M., Otsuka, Y., and Saito, A.: Vertical connection from the
tropospheric activities to the ionospheric longitudinal structure simulated by a new Earth’s whole atmosphere-ionosphere coupled model,
J. Geophys. Res.: Space Physics, 116, <https://doi.org/10.1029/2010JA015925>, 2011.
- Jin, H., Miyoshi, Y., Pancheva, D., Mukhtarov, P., Fujiwara, H., and Shinagawa, H.: Response of migrating tides to the stratospheric sud-
495 den warming in 2009 and their effects on the ionosphere studied by a whole atmosphere-ionosphere model GAIA with COSMIC and
TIMED/SABER observations, *J. Geophys. Res.: Space Physics*, 117, <https://doi.org/10.1029/2012JA017650>, 2012.
- Kasahara, A.: Normal modes of ultralong waves in the atmosphere, *Mon. Weather Rev.*, 104, 669–690, [https://doi.org/10.1175/1520-0493\(1976\)104<0669:NMOUWI>2.0.CO;2](https://doi.org/10.1175/1520-0493(1976)104<0669:NMOUWI>2.0.CO;2), 1976.
- Kikuchi, K.: An introduction to combined Fourier–wavelet transform and its application to convectively coupled equatorial waves, *Clim.*
500 *Dyn.*, 43, 1339–1356, <https://doi.org/10.1007/s00382-013-1949-8>, 2014.
- Kikuchi, K. and Wang, B.: Spatiotemporal wavelet transform and the multiscale behavior of the Madden–Julian oscillation, *J. Clim.*, 23,
3814–3834, <https://doi.org/10.1175/2010JCLI2693.1>, 2010.
- Kobayashi, S., Ota, Y., Harada, Y., Ebata, A., Moriya, M., Onoda, H., Onogi, K., Kamahori, H., Kobayashi, C., Endo, H., et al.: The JRA-55
reanalysis: General specifications and basic characteristics, *J. Meteorol. Soc. Japan. Ser. II*, 93, 5–48, <https://doi.org/10.2151/jmsj.2015-001>, 2015.
- 505 Kumar, P. and Fofoula-Georgiou, E.: Wavelet analysis for geophysical applications, *Rev. Geophys.*, 35, 385–412,
<https://doi.org/10.1029/97RG00427>, 1997.
- Laštovička, J.: Forcing of the ionosphere by waves from below, *J. Atmos. Sol.-Terr. Phys.*, 68, 479–497,
<https://doi.org/10.1016/j.jastp.2005.01.018>, 2006.



- 510 Lee, W., Song, I.-S., Kim, J.-H., Kim, Y. H., Jeong, S.-H., Eswaraiah, S., and Murphy, D.: The observation and SD-WACCM simulation of planetary wave activity in the middle atmosphere during the 2019 Southern Hemispheric sudden stratospheric warming, *J. Geophys. Res.: Space Physics*, 126, e2020JA029 094, <https://doi.org/10.1029/2020JA029094>, 2021.
- Lieberman, R., Riggin, D., Ortland, D., Oberheide, J., and Siskind, D.: Global observations and modeling of nonmigrating diurnal tides generated by tide-planetary wave interactions, *J. Geophys. Res.: Atmospheres*, 120, 11–419, <https://doi.org/10.1002/2015JD023739>, 2015.
- 515 Lieberman, R. S. and Riggin, D.: High resolution Doppler imager observations of Kelvin waves in the equatorial mesosphere and lower thermosphere, *J. Geophys. Res.: Atmospheres*, 102, 26 117–26 130, <https://doi.org/10.1029/96JD02902>, 1997.
- Lim, E.-P., Hendon, H. H., Butler, A. H., Garreaud, R. D., Polichtchouk, I., Shepherd, T. G., Scaife, A., Comer, R., Coy, L., Newman, P. A., et al.: The 2019 Antarctic sudden stratospheric warming, *SPARC newsletter*, 54, 10–13, https://www.sparc-climate.org/wp-content/uploads/sites/5/2017/12/SPARCnewsletter_Jan2020_WEB.pdf, 2020.
- 520 Lim, E.-P., Hendon, H. H., Butler, A. H., Thompson, D. W., Lawrence, Z. D., Scaife, A. A., Shepherd, T. G., Polichtchouk, I., Nakamura, H., Kobayashi, C., et al.: The 2019 Southern Hemisphere stratospheric polar vortex weakening and its impacts, *Bull. Am. Meteorol.*, 102, E1150–E1171, <https://doi.org/10.1175/BAMS-D-20-0112.1>, 2021.
- Lin, J., Lin, C., Rajesh, P., Yue, J., Lin, C., and Matsuo, T.: Local-time and vertical characteristics of quasi-6-day oscillation in the ionosphere during the 2019 Antarctic sudden stratospheric warming, *Geophys. Res. Lett.*, 47, e2020GL090 345, <https://doi.org/10.1029/2020GL090345>, 2020.
- 525 Lindzen, R. S. and Chapman, S.: Atmospheric tides, *Space Sci. Rev.*, 10, 3–188, <https://doi.org/doi.org/10.1007/BF00171584>, 1969.
- Liu, H.-L.: WACCM-X simulation of tidal and planetary wave variability in the upper atmosphere, *Modeling the Ionosphere–Thermosphere System*, pp. 181–199, <https://doi.org/10.1002/9781118704417.ch16>, 2014.
- Liu, H.-L.: Variability and predictability of the space environment as related to lower atmosphere forcing, *Space Weather*, 14, 634–658, <https://doi.org/10.1002/2016SW001450>, 2016.
- 530 Liu, H.-L., Talaat, E., Roble, R., Lieberman, R., Riggin, D., and Yee, J.-H.: The 6.5-day wave and its seasonal variability in the middle and upper atmosphere, *J. Geophys. Res.: Atmospheres*, 109, <https://doi.org/10.1029/2004JD004795>, 2004.
- Liu, H.-L., Bardeen, C. G., Foster, B. T., Lauritzen, P., Liu, J., Lu, G., Marsh, D. R., Maute, A., McInerney, J. M., Pedatella, N. M., et al.: Development and validation of the Whole Atmosphere Community Climate Model with thermosphere and ionosphere extension (WACCM-X 2.0), *J. Adv. Model. Earth Syst.*, 10, 381–402, <https://doi.org/10.1002/2017MS001232>, 2018.
- 535 Longuet-Higgins, M. S.: The eigenfunctions of Laplace’s tidal equation over a sphere, *Philos. Trans. R. Soc. A*, 262, 511–607, <https://doi.org/10.1098/rsta.1968.0003>, 1968.
- Lühr, H., Xiong, C., Olsen, N., and Le, G.: Near-Earth magnetic field effects of large-scale magnetospheric currents, *Space Sci. Rev.*, 206, 521–545, <https://doi.org/10.1007/s11214-016-0267-y>, 2017.
- 540 Ma, Z., Gong, Y., Zhang, S., Zhou, Q., Huang, C., Huang, K., Luo, J., Yu, Y., and Li, G.: Study of a Quasi 4-Day Oscillation During the 2018/2019 SSW Over Mohe, China, *J. Geophys. Res.: Space Physics*, 125, e2019JA027 687, <https://doi.org/10.1029/2019JA027687>, 2020.
- Ma, Z., Gong, Y., Zhang, S., Xiao, Q., Huang, C., and Huang, K.: A new methodology for measuring traveling quasi-5-day oscillations during sudden stratospheric warming events based on satellite observations, *Atmos. Chem. Phys.*, 22, 13 725–13 737, <https://doi.org/10.5194/acp-22-13725-2022>, 2022a.
- 545



- Ma, Z., Gong, Y., Zhang, S., Xiao, Q., Xue, J., Huang, C., and Huang, K.: Understanding the Excitation of Quasi-6-Day Waves in Both Hemispheres During the September 2019 Antarctic SSW, *J. Geophys. Res.: Atmospheres*, 127, e2021JD035984, <https://doi.org/10.1029/2021JD035984>, 2022b.
- Madden, R. A.: Large-scale, free Rossby waves in the atmosphere—An update, *Tellus A*, 59, 571–590, <https://doi.org/10.1111/j.1600-0870.2007.00257.x>, 2007.
- 550
- Manney, G. L., Schwartz, M. J., Krüger, K., Santee, M. L., Pawson, S., Lee, J. N., Daffer, W. H., Fuller, R. A., and Livesey, N. J.: Aura Microwave Limb Sounder observations of dynamics and transport during the record-breaking 2009 Arctic stratospheric major warming, *Geophys. Res. Lett.*, 36, <https://doi.org/10.1029/2009GL038586>, 2009.
- Matsuno, T.: Quasi-geostrophic motions in the equatorial area, *J. Meteorol. Soc. Japan. Ser. II*, 44, 25–43, https://doi.org/10.2151/jmsj1965.44.1_25, 1966.
- 555
- Maus, S., Rother, M., Hemant, K., Stolle, C., Lühr, H., Kuvshinov, A., and Olsen, N.: Earth’s lithospheric magnetic field determined to spherical harmonic degree 90 from CHAMP satellite measurements, *Geophys. J. Int.*, 164, 319–330, <https://doi.org/10.1111/j.1365-246X.2005.02833.x>, 2006.
- McDonald, A., Hibbins, R., and Jarvis, M.: Properties of the quasi 16 day wave derived from EOS MLS observations, *J. Geophys. Res.: Atmospheres*, 116, <https://doi.org/10.1029/2010JD014719>, 2011.
- 560
- Mechoso, C. R. and Hartmann, D. L.: An observational study of traveling planetary waves in the Southern Hemisphere, *J. Atmos. Sci.*, 39, 1921–1935, [https://doi.org/10.1175/1520-0469\(1982\)039<1921:AOSOTP>2.0.CO;2](https://doi.org/10.1175/1520-0469(1982)039<1921:AOSOTP>2.0.CO;2), 1982.
- Meyers, S. D., Kelly, B. G., and O’Brien, J. J.: An introduction to wavelet analysis in oceanography and meteorology: With application to the dispersion of Yanai waves, *Mon. Weather Rev.*, 121, 2858–2866, [https://doi.org/10.1175/1520-0493\(1993\)121<2858:AITWAI>2.0.CO;2](https://doi.org/10.1175/1520-0493(1993)121<2858:AITWAI>2.0.CO;2),
- 565 1993.
- Mitra, G., Guharay, A., Batista, P. P., and Buriti, R.: Impact of the September 2019 Minor Sudden Stratospheric Warming on the Low-Latitude Middle Atmospheric Planetary Wave Dynamics, *J. Geophys. Res.: Atmospheres*, 127, e2021JD035538, <https://doi.org/10.1029/2021JD035538>, 2022.
- Miyoshi, Y.: Temporal variation of nonmigrating diurnal tide and its relation with the moist convective activity, *Geophys. Res. Lett.*, 33, <https://doi.org/10.1029/2006GL026072>, 2006.
- 570
- Miyoshi, Y. and Fujiwara, H.: Day-to-day variations of migrating diurnal tide simulated by a GCM from the ground surface to the exobase, *Geophys. Res. Lett.*, 30, <https://doi.org/10.1029/2003GL017695>, 2003.
- Miyoshi, Y. and Fujiwara, H.: Excitation mechanism of intraseasonal oscillation in the equatorial mesosphere and lower thermosphere, *J. Geophys. Res.: Atmospheres*, 111, <https://doi.org/10.1029/2003GL017695>, 2006.
- 575
- Miyoshi, Y. and Yamazaki, Y.: Excitation mechanism of ionospheric 6-day oscillation during the 2019 September sudden stratospheric warming event, *J. Geophys. Res.: Space Physics*, 125, e2020JA028283, <https://doi.org/10.1029/2020JA028283>, 2020.
- Miyoshi, Y., Pancheva, D., Mukhtarov, P., Jin, H., Fujiwara, H., and Shinagawa, H.: Excitation mechanism of non-migrating tides, *J. Atmos. Sol.-Terr. Phys.*, 156, 24–36, <https://doi.org/10.1016/j.jastp.2017.02.012>, 2017.
- Moldwin, M.: An introduction to space weather, Cambridge University Press, <https://doi.org/10.1017/CBO9780511801365>, 2022.
- 580
- Moudden, Y. and Forbes, J.: Quasi-two-day wave structure, interannual variability, and tidal interactions during the 2002–2011 decade, *J. Geophys. Res.: Atmospheres*, 119, 2241–2260, <https://doi.org/10.1002/2013JD020563>, 2014.
- Mukhtarov, P., Andonov, B., Borries, C., Pancheva, D., and Jakowski, N.: Forcing of the ionosphere from above and below during the Arctic winter of 2005/2006, *J. Atmos. Sol.-Terr. Phys.*, 72, 193–205, <https://doi.org/10.1016/j.jastp.2009.11.008>, 2010.



- 585 Noguchi, S., Kuroda, Y., Kodera, K., and Watanabe, S.: Robust enhancement of tropical convective activity by the 2019 Antarctic sudden stratospheric warming, *Geophys. Res. Lett.*, 47, e2020GL088743, <https://doi.org/10.1029/2020GL088743>, 2020.
- Oberheide, J., Forbes, J., Häusler, K., Wu, Q., and Bruinsma, S.: Tropospheric tides from 80 to 400 km: Propagation, interannual variability, and solar cycle effects, *J. Geophys. Res.: Atmospheres*, 114, <https://doi.org/10.1029/2009JD012388>, 2009.
- Oberheide, J., Forbes, J., Zhang, X., and Bruinsma, S.: Climatology of upward propagating diurnal and semidiurnal tides in the thermosphere, *J. Geophys. Res.: Space Physics*, 116, <https://doi.org/10.1029/2011JA016784>, 2011.
- 590 Olsen, N. and Stolle, C.: Satellite geomagnetism, *Annu. Rev. Earth Planet Sci.*, 40, 441–465, <https://doi.org/10.1146/annurev-earth-042711-105540>, 2012.
- Palo, S., Forbes, J., Zhang, X., Russell Iii, J., and Mlynczak, M.: An eastward propagating two-day wave: Evidence for nonlinear planetary wave and tidal coupling in the mesosphere and lower thermosphere, *Geophys. Res. Lett.*, 34, <https://doi.org/10.1029/2006GL027728>, 2007.
- 595 Pancheva, D. and Mukhtarov, P.: Strong evidence for the tidal control on the longitudinal structure of the ionospheric F-region, *Geophys. Res. Lett.*, 37, <https://doi.org/10.1029/2010GL044039>, 2010.
- Pancheva, D., Mukhtarov, P., and Siskind, D. E.: The quasi-6-day waves in NOGAPS-ALPHA forecast model and their climatology in MLS/Aura measurements (2005–2014), *J. Atmos. Sol.-Terr. Phys.*, 181, 19–37, <https://doi.org/10.1016/j.jastp.2018.10.008>, 2018.
- Pedatella, N., Liu, H.-L., and Hagan, M.: Day-to-day migrating and nonmigrating tidal variability due to the six-day planetary wave, *J. Geophys. Res.: Space Physics*, 117, <https://doi.org/10.1029/2012JA017581>, 2012a.
- 600 Pedatella, N., Liu, H.-L., Richmond, A., Maute, A., and Fang, T.-W.: Simulations of solar and lunar tidal variability in the mesosphere and lower thermosphere during sudden stratosphere warmings and their influence on the low-latitude ionosphere, *J. Geophys. Res.: Space Physics*, 117, <https://doi.org/10.1029/2012JA017792>, 2012b.
- Pedatella, N., Liu, H.-L., Sassi, F., Lei, J., Chau, J., and Zhang, X.: Ionosphere variability during the 2009 SSW: Influence of the lunar semidiurnal tide and mechanisms producing electron density variability, *J. Geophys. Res.: Space Physics*, 119, 3828–3843, <https://doi.org/10.1002/2014JA019849>, 2014.
- 605 Pedatella, N., Chau, J., Schmidt, H., Goncharenko, L., Stolle, C., Hocke, K., Harvey, V., Funke, B., and Siddiqui, T.: How Sudden stratospheric warmings affect the whole atmosphere, *EOS*, <https://doi.org/10.1029/2018EO092441>, 2018.
- Pogoreltsev, A., Fedulina, I., Mitchell, N., Muller, H., Luo, Y., Meek, C., and Manson, A.: Global free oscillations of the atmosphere and secondary planetary waves in the mesosphere and lower thermosphere region during August/September time conditions, *J. Geophys. Res.: Atmospheres*, 107, ACL–24, <https://doi.org/10.1029/2001JD001535>, 2002.
- 610 Qin, Y., Gu, S.-Y., and Dou, X.: A New Mechanism for the Generation of Quasi-6-Day and Quasi-10-Day Waves During the 2019 Antarctic Sudden Stratospheric Warming, *J. Geophys. Res.: Atmospheres*, 126, e2021JD035568, <https://doi.org/10.1029/2021JD035568>, 2021a.
- Qin, Y., Gu, S.-Y., Teng, C.-K.-M., Dou, X.-K., Yu, Y., and Li, N.: Comprehensive study of the climatology of the quasi-6-day wave in the MLT region based on Aura/MLS observations and SD-WACCM-X simulations, *J. Geophys. Res.: Space Physics*, 126, e2020JA028454, <https://doi.org/10.1029/2020JA028454>, 2021b.
- 615 Qin, Y., Gu, S.-Y., Dou, X., Teng, C.-K.-M., Yang, Z., and Sun, R.: Southern Hemisphere Response to the Secondary Planetary Waves Generated During the Arctic Sudden Stratospheric Final Warmings: Influence of the Quasi-Biennial Oscillation, *J. Geophys. Res.: Atmospheres*, p. e2022JD037730, <https://doi.org/10.1029/2022JD037730>, 2022.
- 620 Rao, J., Garfinkel, C. I., White, I. P., and Schwartz, C.: The Southern Hemisphere minor sudden stratospheric warming in September 2019 and its predictions in S2S models, *J. Geophys. Res.: Atmospheres*, 125, e2020JD032723, <https://doi.org/10.1029/2020JD032723>, 2020.



- Safieddine, S., Bouillon, M., Paracho, A.-c., Jumelet, J., Tence, F., Pazmino, A., Goutail, F., Wespes, C., Bekki, S., Boynard, A., et al.: Antarctic ozone enhancement during the 2019 sudden stratospheric warming event, *Geophys. Res. Lett.*, 47, e2020GL087810, <https://doi.org/10.1029/2020GL087810>, 2020.
- 625 Salby, M. L.: The 2-day wave in the middle atmosphere: Observations and theory, *J. Geophys. Res.: Oceans*, 86, 9654–9660, <https://doi.org/10.1029/JC086iC10p09654>, 1981a.
- Salby, M. L.: Rossby normal modes in nonuniform background configurations. Part I: Simple fields, *J. Atmos. Sci.*, 38, 1803–1826, [https://doi.org/10.1175/1520-0469\(1981\)038<1803:RNMINB>2.0.CO;2](https://doi.org/10.1175/1520-0469(1981)038<1803:RNMINB>2.0.CO;2), 1981b.
- Salby, M. L.: Rossby normal modes in nonuniform background configurations. Part II. Equinox and solstice conditions, *J. Atmos. Sci.*, 38, 1827–1840, [https://doi.org/10.1175/1520-0469\(1981\)038<1827:RNMINB>2.0.CO;2](https://doi.org/10.1175/1520-0469(1981)038<1827:RNMINB>2.0.CO;2), 1981c.
- 630 Salby, M. L.: Survey of planetary-scale traveling waves: The state of theory and observations, *Rev. Geophys.*, 22, 209–236, <https://doi.org/10.1029/RG022i002p00209>, 1984.
- Salby, M. L. and Callaghan, P. F.: Seasonal amplification of the 2-day wave: Relationship between normal mode and instability, *J. Atmos. Sci.*, 58, 1858–1869, [https://doi.org/10.1175/1520-0469\(2001\)058<1858:SAOTDW>2.0.CO;2](https://doi.org/10.1175/1520-0469(2001)058<1858:SAOTDW>2.0.CO;2), 2001.
- 635 Sassi, F., Garcia, R., and Hoppel, K.: Large-scale Rossby normal modes during some recent Northern Hemisphere winters, *J. Atmos. Sci.*, 69, 820–839, <https://doi.org/10.1175/JAS-D-11-0103.1>, 2012.
- Sassi, F., Liu, H.-L., Ma, J., and Garcia, R. R.: The lower thermosphere during the Northern Hemisphere winter of 2009: A modeling study using high-altitude data assimilation products in WACCM-X, *J. Geophys. Res.: Atmospheres*, 118, 8954–8968, <https://doi.org/10.1002/jgrd.50632>, 2013.
- 640 Sassi, F., Liu, H.-L., and Emmert, J. T.: Traveling planetary-scale waves in the lower thermosphere: Effects on neutral density and composition during solar minimum conditions, *J. Geophys. Res.: Space Physics*, 121, 1780–1801, <https://doi.org/10.1002/2015JA022082>, 2016.
- Schunk, R. and Sojka, J. J.: Ionosphere-thermosphere space weather issues, *J. Atmos. Terr. Phys.*, 58, 1527–1574, [https://doi.org/10.1016/0021-9169\(96\)00029-3](https://doi.org/10.1016/0021-9169(96)00029-3), 1996.
- Siddiqui, T., Maute, A., and Pedatella, N.: On the importance of interactive ozone chemistry in Earth-system models for studying mesosphere-lower thermosphere tidal changes during sudden stratospheric warmings, *J. Geophys. Res.: Space Physics*, 124, 10 690–10 707, <https://doi.org/10.1029/2019JA027193>, 2019.
- Siddiqui, T., Yamazaki, Y., Stolle, C., Maute, A., Laštovička, J., Edemskiy, I., Mošna, Z., and Sivakandan, M.: Understanding the total electron content variability over Europe during 2009 and 2019 SSWs, *J. Geophys. Res.: Space Physics*, 126, e2020JA028751, <https://doi.org/10.1029/2020JA028751>, 2021.
- 650 Siddiqui, T. A., Chau, J. L., Stolle, C., and Yamazaki, Y.: Migrating solar diurnal tidal variability during Northern and Southern Hemisphere Sudden Stratospheric Warmings, *Earth, Planets and Space*, 74, 1–17, <https://doi.org/10.1186/s40623-022-01661-y>, 2022.
- Sobkhiz-Miandehi, S., Yamazaki, Y., Arras, C., Miyoshi, Y., and Shinagawa, H.: Comparison of the tidal signatures in sporadic E and vertical ion convergence rate, using FORMOSAT-3/COSMIC radio occultation observations and GAIA model, *Earth, Planets and Space*, 74, 1–13, <https://doi.org/10.1186/s40623-022-01637-y>, 2022.
- 655 Thébault, E., Vigneron, P., Langlais, B., and Hulot, G.: A Swarm lithospheric magnetic field model to SH degree 80, *Earth, Planets and Space*, 68, 1–13, <https://doi.org/10.1186/s40623-016-0510-5>, 2016.
- Torrence, C. and Compo, G. P.: A practical guide to wavelet analysis, *Bull. Am. Meteorol.*, 79, 61–78, [https://doi.org/10.1175/1520-0477\(1998\)079<0061:APGTWA>2.0.CO;2](https://doi.org/10.1175/1520-0477(1998)079<0061:APGTWA>2.0.CO;2), 1998.



- 660 Wang, H., Akmaev, R., Fang, T.-W., Fuller-Rowell, T., Wu, F., Maruyama, N., and Iredell, M.: First forecast of a sudden strato-
spheric warming with a coupled whole-atmosphere/ionosphere model IDEA, *J. Geophys. Res.: Space Physics*, 119, 2079–2089,
<https://doi.org/10.1002/2013JA019481>, 2014.
- Wang, J. C., Palo, S. E., Forbes, J., Marino, J., Moffat-Griffin, T., and Mitchell, N.: Unusual quasi 10-day planetary wave activity and
the ionospheric response during the 2019 Southern Hemisphere sudden stratospheric warming, *J. Geophys. Res.: Space Physics*, 126,
e2021JA029286, <https://doi.org/10.1029/2021JA029286>, 2021a.
- 665 Wang, J. C., Palo, S. E., Liu, H.-L., and Siskind, D.: Day-to-Day Variability of Diurnal Tide in the Mesosphere and Lower Thermosphere
Driven From Below, *J. Geophys. Res.: Space Physics*, 126, e2019JA027759, <https://doi.org/10.1029/2019JA027759>, 2021b.
- Wargan, K., Weir, B., Manney, G. L., Cohn, S. E., and Livesey, N. J.: The anomalous 2019 Antarctic ozone hole in the
GEOS Constituent Data Assimilation System with MLS observations, *J. Geophys. Res.: Atmospheres*, 125, e2020JD033335,
<https://doi.org/10.1029/2020JD033335>, 2020.
- 670 Wells, D. E., Vaníček, P., and Pagiatakis, S. D.: Least squares spectral analysis revisited, Tech. rep., Department of Surveying Engineering,
University of New Brunswick Fredericton, N.B., Canada, <https://gge.ext.unb.ca/Pubs/TR84.pdf>, 1985.
- Wheeler, M. and Kiladis, G. N.: Convectively coupled equatorial waves: Analysis of clouds and temperature in the wavenumber–frequency
domain, *J. Atmos. Sci.*, 56, 374–399, [https://doi.org/10.1175/1520-0469\(1999\)056<0374:CCEWAO>2.0.CO;2](https://doi.org/10.1175/1520-0469(1999)056<0374:CCEWAO>2.0.CO;2), 1999.
- Wu, D., Hays, P., Skinner, W., Marshall, A., Burrage, M., Lieberman, R., and Ortlund, D.: Observations of the quasi 2-day wave from the
675 High Resolution Doppler Imager on UARS, *Geophys. Res. Lett.*, 20, 2853–2856, <https://doi.org/10.1029/93GL03008>, 1993.
- Wu, D., Hays, P., and Skinner, W.: Observations of the 5-day wave in the mesosphere and lower thermosphere, *Geophys. Res. Lett.*, 21,
2733–2736, <https://doi.org/10.1016/j.jastp.2005.05.010>, 1994.
- Yamazaki, Y.: Quasi-6-day wave effects on the equatorial ionization anomaly over a solar cycle, *J. Geophys. Res.: Space Physics*, 123,
9881–9892, <https://doi.org/10.1029/2018JA026014>, 2018.
- 680 Yamazaki, Y. and Matthias, V.: Large-amplitude quasi-10-day waves in the middle atmosphere during final warmings, *J. Geophys. Res.:*
Atmospheres, 124, 9874–9892, <https://doi.org/10.1029/2019JD030634>, 2019.
- Yamazaki, Y., Matthias, V., Miyoshi, Y., Stolle, C., Siddiqui, T., Kervalishvili, G., Laštovička, J., Kozubek, M., Ward, W., Themens, D. R.,
et al.: September 2019 Antarctic sudden stratospheric warming: Quasi-6-day wave burst and ionospheric effects, *Geophys. Res. Lett.*, 47,
e2019GL086577, <https://doi.org/10.1029/2019GL086577>, 2020a.
- 685 Yamazaki, Y., Miyoshi, Y., Xiong, C., Stolle, C., Soares, G., and Yoshikawa, A.: Whole atmosphere model simulations of ul-
trafast Kelvin wave effects in the ionosphere and thermosphere, *J. Geophys. Res.: Space Physics*, 125, e2020JA027939,
<https://doi.org/10.1029/2020JA027939>, 2020b.
- Yamazaki, Y., Matthias, V., and Miyoshi, Y.: Quasi-4-Day Wave: Atmospheric Manifestation of the First Symmetric Rossby Normal Mode
of Zonal Wavenumber 2, *J. Geophys. Res.: Atmospheres*, 126, e2021JD034855, <https://doi.org/10.1029/2021JD034855>, 2021.
- 690 Yiğit, E. and Medvedev, A. S.: Internal wave coupling processes in Earth’s atmosphere, *Adv. Space Res.*, 55, 983–1003,
<https://doi.org/10.1016/j.asr.2014.11.020>, 2015.
- Yin, S., Ma, Z., Gong, Y., Zhang, S., and Li, G.: Response of quasi-10-day waves in the MLT region to the sudden stratospheric warming in
March 2020, *Adv. Space Res.*, <https://doi.org/doi.org/10.1016/j.asr.2022.10.054>, 2022.
- Yu, F. R., Huang, K. M., Zhang, S. D., Huang, C. M., Yi, F., Gong, Y., Wang, R., Li, G., and Ning, B.: Quasi 10-and 16-day wave activities
695 observed through meteor radar and MST radar during stratospheric final warming in 2015 spring, *J. Geophys. Res.: Atmospheres*, 124,
6040–6056, <https://doi.org/10.1029/2019JD030630>, 2019.



- Yue, J., Liu, H.-L., and Chang, L. C.: Numerical investigation of the quasi 2 day wave in the mesosphere and lower thermosphere, *J. Geophys. Res.: Atmospheres*, 117, <https://doi.org/10.1029/2011JD016574>, 2012.
- 700 Yue, X., Schreiner, W. S., Lei, J., Rocken, C., Hunt, D. C., Kuo, Y.-H., and Wan, W.: Global ionospheric response observed by COSMIC satellites during the January 2009 stratospheric sudden warming event, *J. Geophys. Res.: Space Physics*, 115, <https://doi.org/10.1029/2010JA015466>, 2010.
- Zhang, X., Forbes, J. M., Hagan, M. E., Russell III, J. M., Palo, S. E., Mertens, C. J., and Mlynchzak, M. G.: Monthly tidal temperatures 20–120 km from TIMED/SABER, *J. Geophys. Res.: Space Physics*, 111, <https://doi.org/10.1029/2005JA011504>, 2006.
- 705 Zhao, Y., Taylor, M. J., Pautet, P.-D., Moffat-Griffin, T., Hervig, M. E., Murphy, D. J., French, W., Liu, H.-L., Pendleton Jr, W. R., and Russell III, J.: Investigating an unusually large 28-day oscillation in mesospheric temperature over Antarctica using ground-based and satellite measurements, *J. Geophys. Res.: Atmospheres*, 124, 8576–8593, <https://doi.org/10.1029/2019JD030286>, 2019.

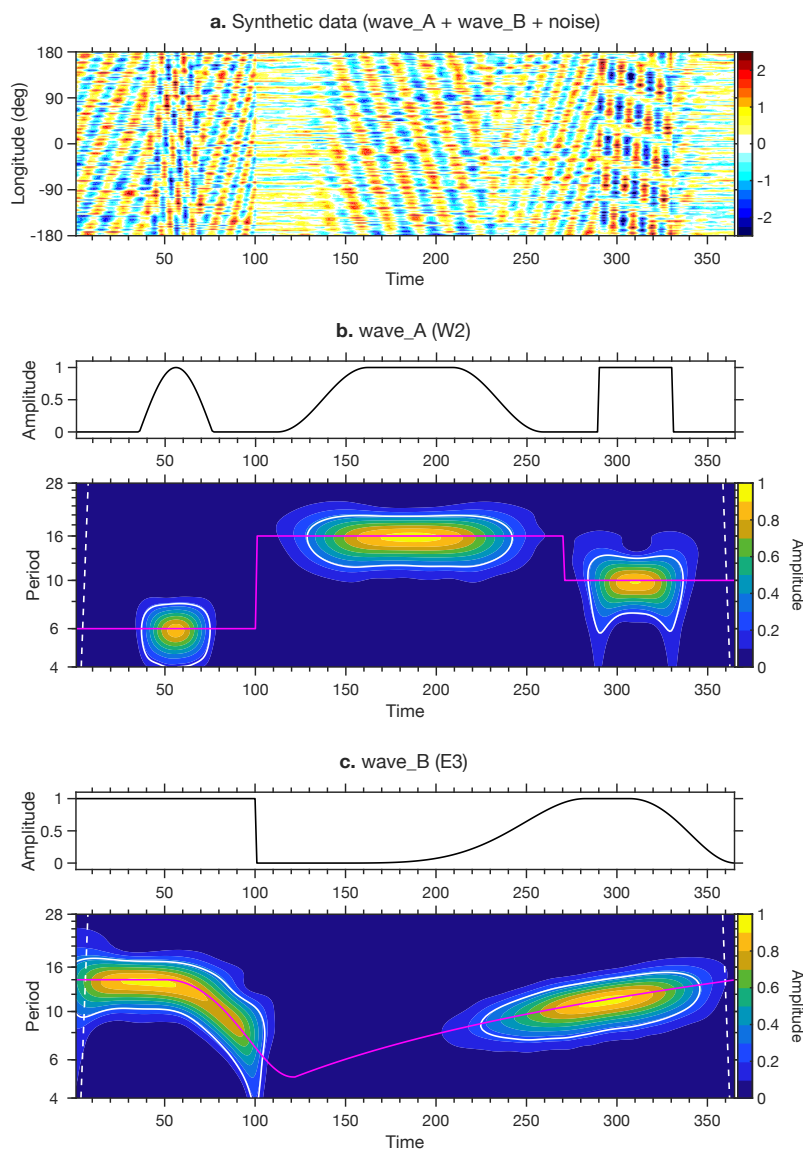


Figure 1. (a) Synthetic data containing wave_A (westward-propagating with zonal wavenumber 2, W2) and wave_B (eastward-propagating with zonal wavenumber 3, E3), along with noise. (b) Amplitude and phase of wave_A. The upper panel shows the amplitude, and the lower panel shows the phase (magenta line). The lower panel also shows the combined Fourier-wavelet (CFW) amplitude spectrum for W2. The white curves indicate the 95% confidence level, while the white dashed lines show the cone of influence. (c) Same as (b) except for wave_B. The lower panel shows the CFW spectrum for E3.



GAIA

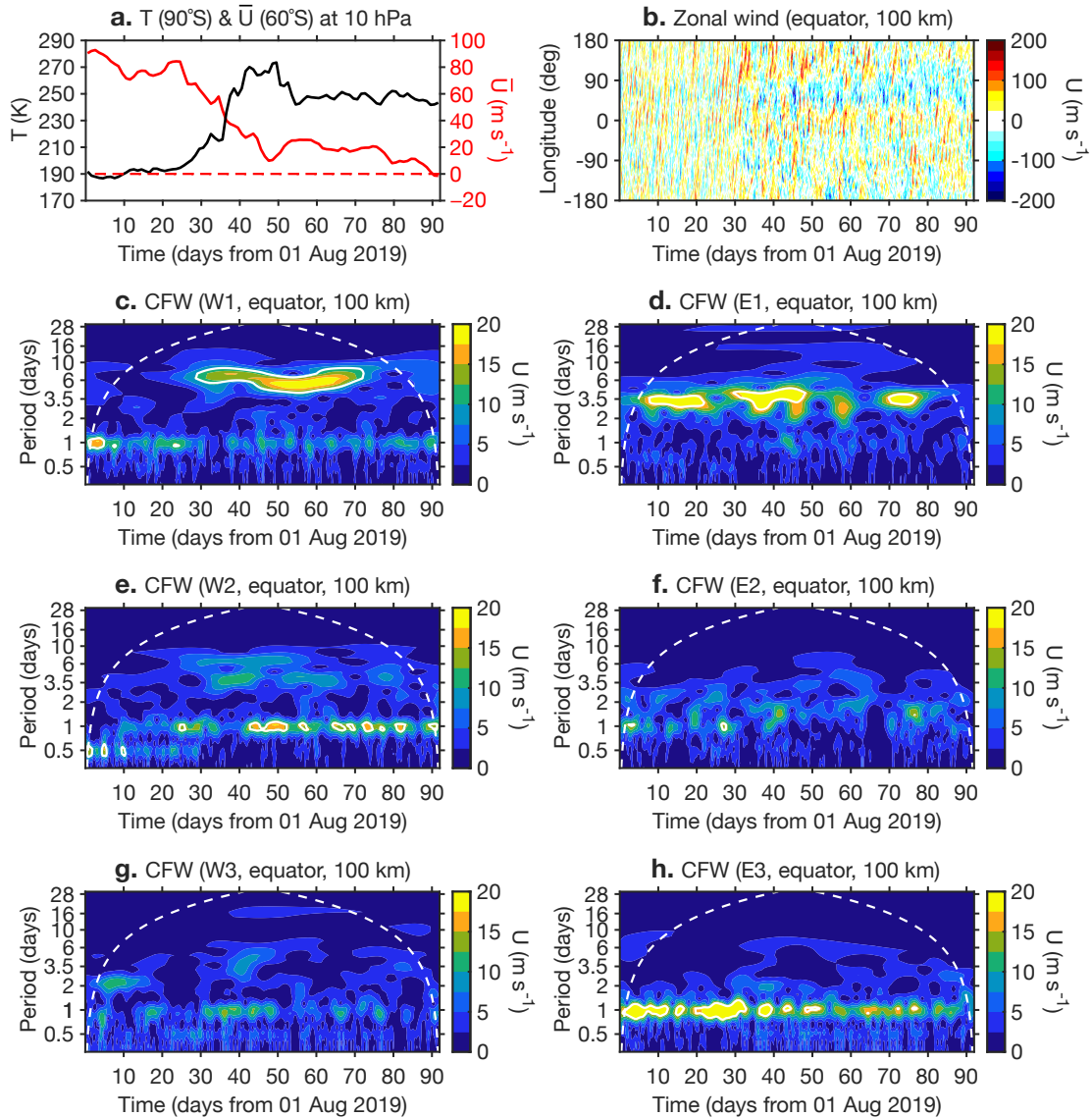


Figure 2. GAIA model simulation for the period August–October 2019. (a) Polar temperature and zonal mean zonal wind velocity at 60°N at 10 hPa. (b) Zonal wind velocity over the equator at a height of 100 km. (c–h) Combined Fourier-wavelet (CFW) spectra of the equatorial zonal wind velocity at 100 km for (c) the westward-propagating zonal wavenumber 1 (W1) component, (d) the eastward-propagating zonal wavenumber 1 (E1) component, (e) the westward-propagating zonal wavenumber 2 (W2) component, (f) the eastward-propagating zonal wavenumber 2 (E2) component, (g) the westward-propagating zonal wavenumber 3 (W3) component and (h) the eastward-propagating zonal wavenumber 3 (E3) component. The white curves indicate the 95% confidence level, while the white dashed lines show the cone of influence.

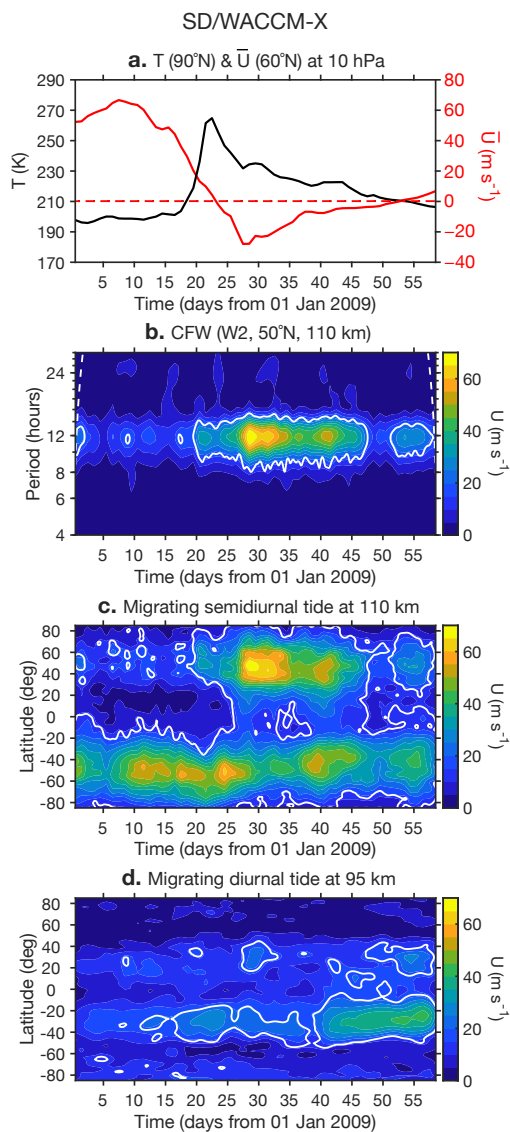


Figure 3. SD/WACCM-X model simulation for the period January–February 2009. (a) Polar temperature and zonal mean zonal wind velocity at 60°N at 10 hPa. (b) Combined Fourier-wavelet (CFW) spectrum of the zonal wind velocity at 50°N and 110 km. The white curves indicate the 95% confidence level, while the white dashed lines show the cone of influence. (c) Amplitude of the migrating semidiurnal tide in the zonal wind velocity at 110 km as determined by the CFW technique. (d) Amplitude of the migrating diurnal tide in the zonal wind velocity at 95 km as determined by the CFW technique.

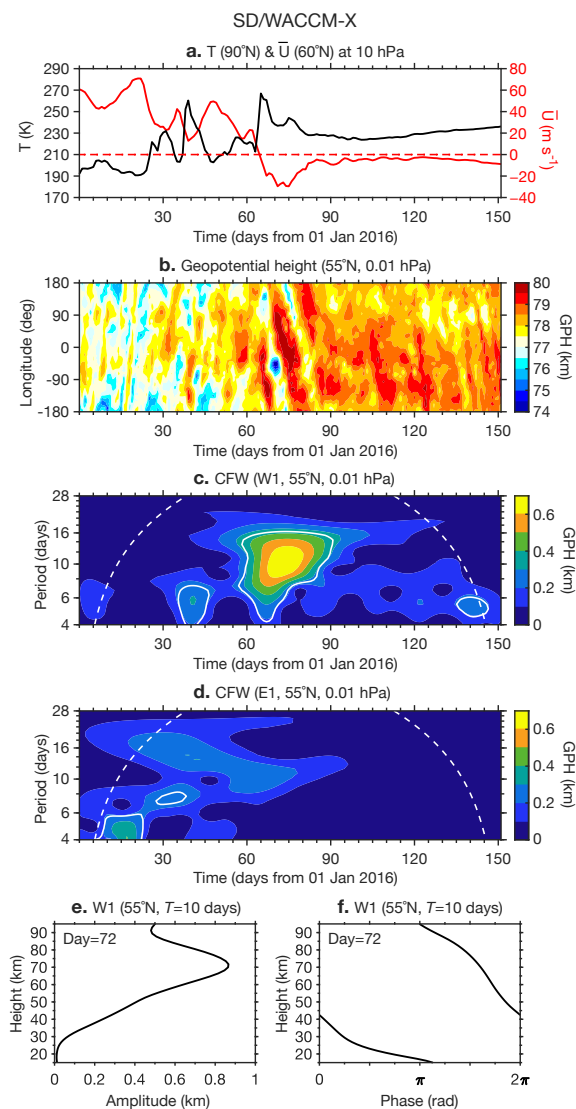


Figure 4. SD/WACCM-X model simulation for the period January–May 2016. (a) Polar temperature and zonal mean zonal wind velocity at 60°N at 10 hPa. (b) Geopotential height at 55°N at 0.01 hPa. (c–d) Combined Fourier-wavelet (CFW) spectra of the geopotential height at 55°N at 0.01 hPa for (c) the westward-propagating zonal wavenumber 1 (W1) component and (d) the eastward-propagating zonal wavenumber 1 (E1) component. (e–f) Height profiles of (e) amplitude and (f) phase of the W1 component at a period of 10 days at 55°N and 0.01 hPa on Day 72 as determined by the CFW technique.

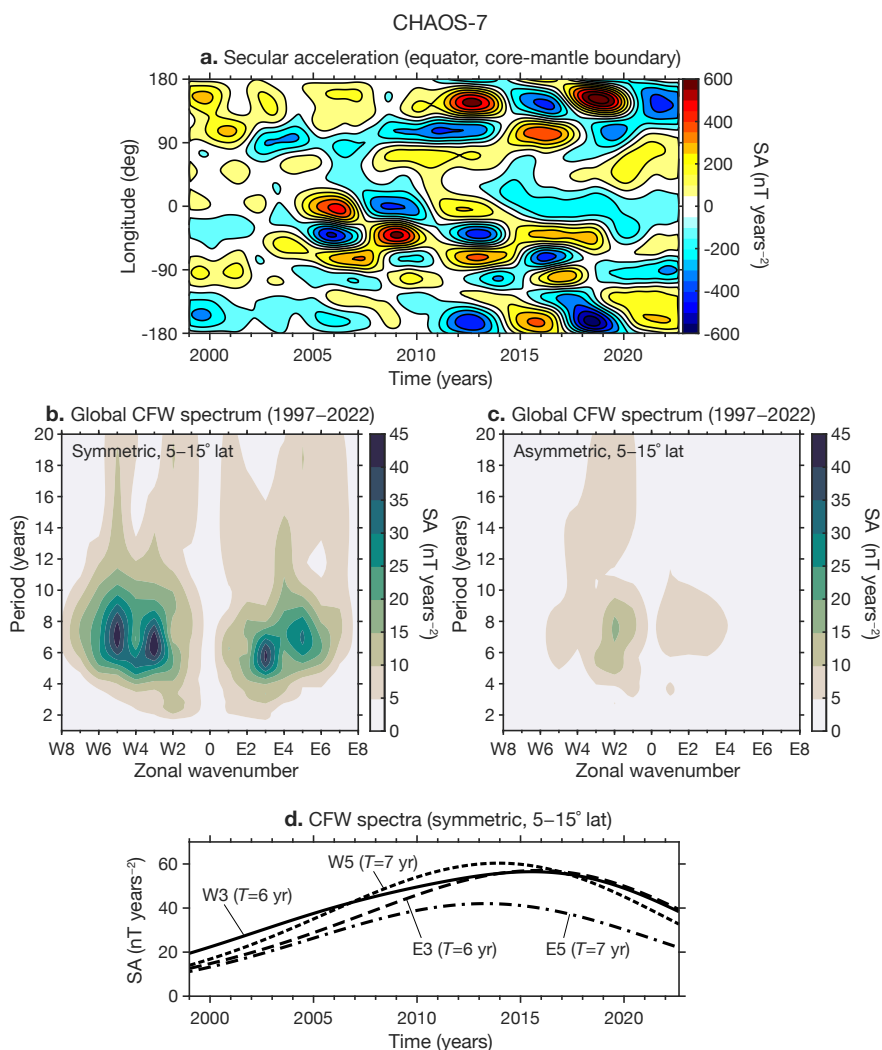


Figure 5. (a) CHAOS-7 model prediction of the secular acceleration (SA) in the radial component of the geomagnetic field at the core-mantle boundary over the equator for the period 1997–2022. (b) Global combined Fourier-wavelet (CFW) spectrum for the equatorially symmetric part of SA for 1997–2022. (c) Same as (b) but for the equatorially asymmetric part of SA. (d) Amplitude of the eastward- and westward-propagating zonal wavenumber 3 components (E3 and W3, respectively) of SA at a period of 6 years, and amplitude of the eastward- and westward-propagating zonal wavenumber 5 components (E5 and W5, respectively) of SA at a period of 7 years as determined by the CFW technique.